Bioactive Materials 36 (2024) 185–202

Contents lists available at ScienceDirect

Bioactive Materials

journal homepage: www.keaipublishing.com/en/journals/bioactive-materials

Cell-homing and immunomodulatory composite hydrogels for effective wound healing with neovascularization

Hayeon Byun [a,b,1], Yujin Han [a,1], Eunhyung Kim [a], Indong Jun [c], Jinkyu Lee [a], Hyewoo Jeong [a], Seung Jae Huh [a], Jinmyoung Joo [d], Su Ryon Shin [b], Heungsoo Shin [a,e,*]

[a] Department of Bioengineering, Hanyang University, 222 Wangsimni-ro, Seongdong-gu, Seoul 04763, Republic of Korea
[b] Division of Engineering in Medicine, Department of Medicine, Harvard Medical School, Brigham and Women's Hospital, Cambridge, MA 02139, USA
[c] Environmental Safety Group, Korea Institute of Science & Technology Europe (KIST-EUROPE), Saarbrücken 66123, Germany
[d] Department of Biomedical Engineering, Ulsan National Institute of Science and Technology (UNIST), Ulsan 44919, Republic of Korea
[e] Institute of Nano Science and Technology, Hanyang University, 222 Wangsimni-ro, Seongdong-gu, Seoul 04763, Republic of Korea

ARTICLE INFO

Keywords:
Immunomodulation
Wound healing
Neovascularization
Multi-functional nanoparticles
Composite hydrogels

ABSTRACT

Wound healing in cases of excessive inflammation poses a significant challenge due to compromised neovascularization. Here, we propose a multi-functional composite hydrogel engineered to overcome such conditions through recruitment and activation of macrophages with adapted degradation of the hydrogel. The composite hydrogel (G-TSrP) is created by combining gelatin methacryloyl (GelMA) and nanoparticles (TSrP) composed of tannic acid (TA) and Sr^{2+}. These nanoparticles are prepared using a one-step mineralization process assisted by metal-phenolic network formation. G-TSrP exhibits the ability to eliminate reactive oxygen species and direct polarization of macrophages toward M2 phenotype. It has been observed that the liberation of TA and Sr^{2+} from G-TSrP actively facilitate the recruitment and up-regulation of the expression of extracellular matrix remodeling genes of macrophages, and thereby, coordinate in vivo adapted degradation of the G-TSrP. Most significantly, G-TSrP accelerates angiogenesis despite the TA's inhibitory properties, which are counteracted by the released Sr^{2+}. Moreover, G-TSrP enhances wound closure under inflammation and promotes normal tissue formation with strong vessel growth. Genetic analysis confirms macrophage-mediated wound healing by the composite hydrogel. Collectively, these findings pave the way for the development of biomaterials that promote wound healing by creating regenerative environment.

1. Introduction

Following an injury, the wound healing process encompasses a series of sequential stages, namely hemostasis, inflammation, proliferation, angiogenesis, and tissue remodeling. Each of these stages entails intricate interactions with diverse cell types [1,2]. Macrophages play a pivotal role in regulating the microenvironment of wounds by transforming into either pro-inflammatory M1 macrophages, which are responsible for phagocytosis and inflammation induction, or pro-regenerative M2 macrophages, which contribute to tissue regeneration and vessel formation [3,4]. Extended periods of inflammation in chronic wounds may result in an overpopulation of M1 macrophages, which delays healing process due to impaired neo-vessel formation [5]. In order to promote optimal tissue regeneration and ensure the timely delivery of instructive signals critical for angiogenesis, recruitment and polarization of macrophages must be regulated [6].

Flavonoids have been widely used in biomedical applications due to their beneficial characteristics including anti-bacterial and anti-oxidation properties, and ability to scavenge reactive oxygen species (ROS) [7]. Tannic acid (TA), in particular, exhibits anti-inflammatory effects and can down-regulate M1 polarization in both monocytes and pre-differentiated macrophages, suggesting a potential application in wound healing [8,9]. TA-copper nanoparticles effectively suppressed expression of pro-inflammatory genes and M1 polarization by accelerating wound closure in infected wound models [10]. In addition, TA incorporated into citrate-based hydrogels or used as a surface coating for

Peer review under responsibility of KeAi Communications Co., Ltd.
* Corresponding author. Department of Bioengineering, Hanyang University, 222 Wangsimni-ro, Seongdong-gu, Seoul 04763, Republic of Korea.
E-mail address: hshin@hanyang.ac.kr (H. Shin).
[1] These authors contributed equally to this work.

https://doi.org/10.1016/j.bioactmat.2024.02.029
Received 15 December 2023; Received in revised form 8 February 2024; Accepted 23 February 2024

molybdenum disulfide scaffolds reduced inflammation or partially improved skin regeneration in rat wounds, respectively [11,12]. However, the concern was raised that potent anti-oxidative properties of TA might inadvertently inhibit angiogenesis [13,14]. Human umbilical vein endothelial cells (HUVECs) exhibited substantial reduction in their capacity to generate vascular tubes upon exposure to a TA-diluted medium [15]. In order to harness the unique biological properties of TA, engineering strategies are necessary that concurrently promote the mobility of macrophages and endothelial cells during wound healing cascades.

Metal ions, such as Cu^{2+}, Sr^{2+}, Ca^{2+}, and Mg^{2+}, exhibit an extensive array of biological functions, encompassing anti-bacterial, pro-angiogenic, or pro-osteogenic properties [16,17]. In a chemical context, they form supramolecular assemblies through coordination chemistry with various polyphenols, which renders them valuable constituents for particle fabrication and surface coatings of biomaterials [8,18]. Furthermore, metal ions offer exceptional stability in physiological conditions and lack the toxicity associated with decomposition [19]. Among these metal ions, Sr^{2+} is a regulator that promotes proliferation of endothelial and epithelial cells, ultimately facilitating re-epithelization, which has led to its use in the regeneration of vascularized soft tissue, either through incorporation into scaffolds or forming it as particles [20,21]. For example, the implantation of strontium-coated titanium implants into an in vivo rat tibial model improved the formation of vascularized bone tissue, and microparticles containing strontium-based bioactive glasses were found to induce M2 polarization in mouse monocytes [22,23]. However, the delivery of Sr^{2+} presents challenges. Surface-coating methods tend to have limited delivery efficiency and low quantities of Sr^{2+}, while particle-based delivery may provide sustained ion release but is susceptible to concerns such as in vivo aggregation and rapid clearance [24]. More importantly, the effect of strontium on the migration of macrophages or monocytes during the initial stages of wound healing is not yet fully understood.

Hydrogels have been actively investigated for wound healing due to their low immunogenicity, hydrophilicity, and ability to load and sustain delivery of bioactive biomolecules [25]. However, many hydrogel strategies tend target one facet of the multiple processes of wound healing and often neglect the intricate biological complexities of the early stages of inflammation [26–28]. Ideally, the degradation of hydrogels should coincide with the ingrowth of host tissue. Nonetheless, conventional hydrogels have been designed to avoid foreign-body responses, leading to limited interactions with surrounding tissues, slow degradation, hindered cell infiltration, and restricted vascularization. These circumstances collectively reduced their potential to induce tissue regeneration [29,30]. Although several methods have been devised to enhance hydrogel degradation by adjusting crosslinking density or modifying polymer backbones, these efforts failed to recapitulate natural healing events [31,32].

The ultimate goal of this study was to develop a multi-functional composite hydrogel with the ability to modulate complex immune responses, recruit and polarize macrophages, control the degradation of hydrogels coordinated with cell infiltration, remodel the extracellular matrix (ECM), and induce neo-vessel formation (Fig. 1). We prepared TA-strontium nanoparticles (TSrP) by metal-phenol coordination and incorporated them into a gelatin methacryloyl (GelMA) composite hydrogel (G-TSrP) by UV crosslinking. In vitro analysis revealed the nanoparticles significantly promoted migration of macrophages and M2 polarization, and subsequent in vivo subcutaneous transplantation confirmed augmented hydrogel degradation, robust cell infiltration, and M2 polarization of recruited macrophages. An extension of our investigation to an excessive inflammatory wound healing model validated the regenerative potential of the nanoparticle-incorporated hydrogel to enhance wound

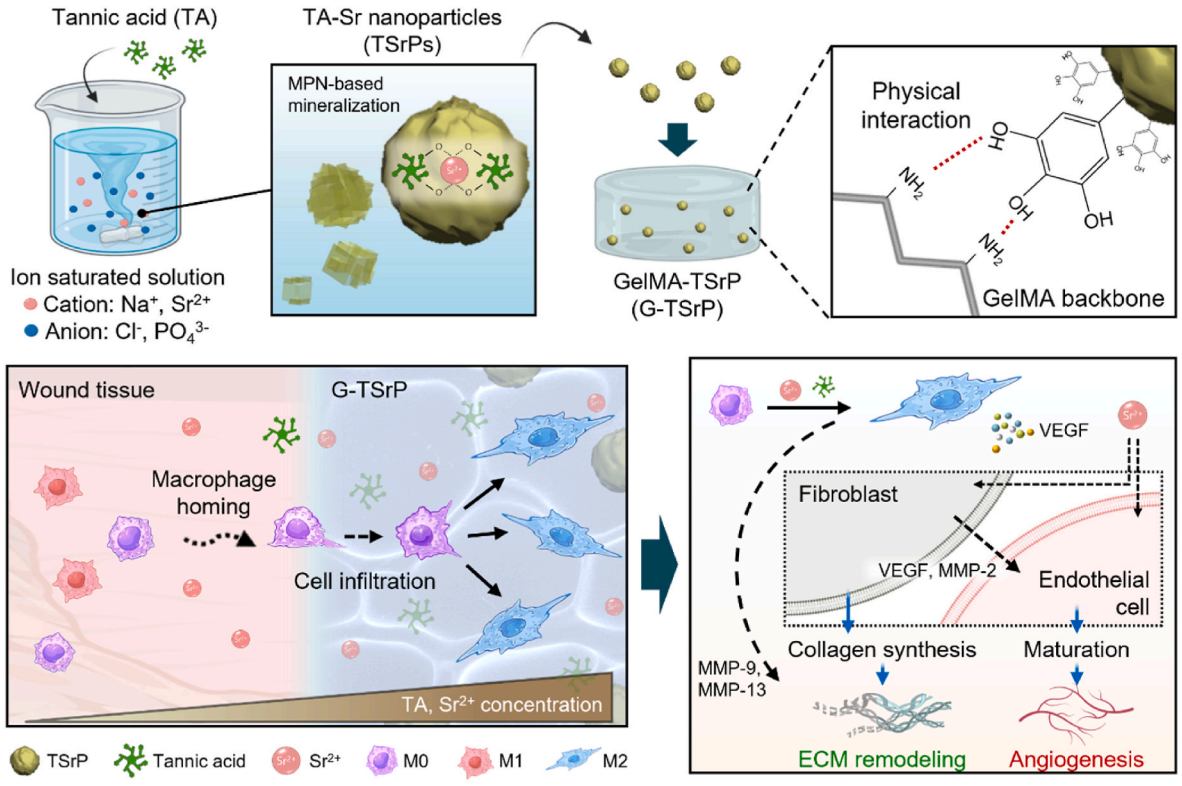

Fig. 1. Schematic illustration of the fabrication of gelatin methacryloyl (GelMA) hydrogel with tannic acid-strontium nanoparticle (G-TSrP) and its wound-healing mechanism. TSrPs were fabricated by mixing tannic acid (TA) with ion-saturated solution in one-step process. The nanoparticles were then incorporated in the GelMA hydrogel via physical interactions. In an inflammatory wound, the G-TSrP releases TA and Sr^{2+} to recruit and polarize macrophages into the M2 state to accelerate regenerative pathway. In addition, the polarized M2 macrophages, along with Sr^{2+}, stimulates fibroblasts and endothelial cells, leading to increased collagen synthesis and matrix metalloproteinase (MMP) secretion, and the maturation of endothelial cells, essential for extracellular matrix (ECM) remodeling and angiogenesis, respectively.

closure, promote the development of an epidermal layer akin to natural skin tissue, increase collagen deposition, and induce neovascularization. Finally, through next-generation sequencing, we substantiated the role of Sr^{2+} and TA in regulating macrophage functionality.

2. Materials and methods

2.1. Materials

Sodium chloride (NaCl) and Strontium chloride hexahydrate ($SrCl_2{\cdot}6H_2O$) were obtained from Junsei (Tokyo, Japan). Sodium phosphate (Na_2HPO_4), TA, Sodium bicarbonate ($NaHCO_3$), Folin-Ciocalteu reagent, 2,2′-azino-bis(3-ethylbenzothiazoline-6-sulfonic acid) diammonium salt (ABTS), Fluorimetric hydrogen peroxide assay kit, 2-Hydroxyl-2-methylpropiophenone, sucrose, silver nitrate, sodium thiosulfate, *o*-Phthaldialdehyde (OPA) reagent, thiazolyl blue tetrazolium bromide (MTT), dimethyl sulfoxide (DMSO), 3% hydrogen peroxide (H_2O_2), Lipopolysaccharide (LPS), 2′,7′-dichlorofluorescein diacetate (DCFDA), Tween-20, Mitomycin C, Crystal violet, Collagenase from *Clostridium histolyticum*, Anti-rabbit immunoglobulin G (IgG) horseradish peroxidase (HRP)-conjugated secondary antibody and secondary anti-mouse, or rabbit IgG biotin-conjugated antibody were purchased from Sigma Aldrich (St.Louis, MO, USA). Frozen section compound was from Leica Biosystems (GmbH, Wetzlar, Germany). Tris HCl was obtained from IBI Scientific (Chavenelle Rd, Dubuque, IA, USA). GelMA (Gelatin from porcine skin, type A, Gel strength: ~300 bloom, Degree of methacrylation: ≥90%) was acquired from 3D Materials (Busan, Korea). Phosphate buffered saline (PBS), Dulbecco's phosphate-buffered saline (DPBS), penicillin streptomycin (P/S), and trypsin/ethylenediaminetetraacetic acid (TE) were from Welgene (Gyeongsan, Korea). Geltrex™, Fetal bovine serum (FBS) and human dermal fibroblasts (HDFBs) were obtained by Gibco™ (Carlsbad, CA, USA). HaCaT cells were acquired from Cell Lines Service (Eppelheim, Germany), and RAW264.7 cells were purchased from the Korean Cell Line Bank (Seoul, Korea). High glucose Dulbecco's modified eagle medium (HGM) and Low glucose Dulbecco's modified eagle medium (LGM) were acquired from SolBio (Suwon, Korea). HUVECs, endothelial basal medium-2 (EBM-2) and endothelial growth medium-2 (EGM-2) were purchased from LONZA (Walkersville, MD, United States). LIVE/DEAD® viability kit, Alexa 488 phalloidin were purchased from Invitrogen (Carlsbad, CA). Human interleukin (IL)-4, and Anti-rabbit IgG Alexa 647-conjugated antibody were from Thermo Fisher Scientific (MA Waltham USA). 4% paraformaldehyde was purchased from Wako (Osaka, Japan), and 4′,6-diamidino-2-phenylindole (DAPI) mounting medium was from Vector Laboratories (Burlingame, CA, USA). Anti-inducible nitric oxide synthase (iNOS) antibody, Anti-CD206 antibody, *Anti*-F4/80 antibody, Anti-wide spectrum cytokeratin antibody, Anti-collagen I (COL I) antibody, *Anti*-α-smooth muscle actin (α-SMA) antibody, Anti-CD31 antibody, Anti-rat IgG biotin-conjugated antibody, and 3,3′-Diaminobenzidine (DAB) substrate kit were acquired from Abcam (Cambridge, UK). Fluorescein isothiocyanate (FITC) streptavidin was obtained from eBioscience (San Diego, CA, USA). The components of real-time quantitative polymerase chain reaction (RT-qPCR); RNeasy Mini Kit, Maxime RT Premix, and SYBR Premix Ex-Taq were purchased from Qiagen (Valencia, CA, USA), Intron (Seoul, Korea), and Takara Bio (Otsu, Japan), respectively. SPLInsert™ (Transwell) was obtained from SPL (Pocheon, Korea). Tegaderm™ and Coban™ were from 3 M (Saint Paul, MN, USA). Harris hematoxylin, Eosin alcoholic Y, and Masson's trichrome stain kit were purchased from BBC Biochemical (Mount Vernon, MA, USA). Wound splint was obtained from Grace Bio-labs (Bend, OR, USA). Dermabond was purchased from Ethicon (Somerset County, NJ, USA). Sirius red/fast green collagen staining kit was obtained from Chondrex (Woodinville, WA, USA).

2.2. One-step fabrication and characterization of nanoparticles

To prepare TSrPs, the 1, 5, and 10 mg/mL of TA were dissolved in ion saturated solution (1 M NaCl, 200 mM $SrCl_2$, and 10 mM Na_2HPO_4 in distilled water (DW), pH 4.35). Then, $NaHCO_3$ (0.04 M) was added to the solution to initiate mineralization with magnetic stirring at 700 rpm for 10 min. The nanoparticles were collected by centrifugation (4000 rpm, 10 min) and re-dispersed in Tris–HCl buffer (pH 8.8) for 10 min at room temperature (RT) to stabilize the particles via deprotonation. Finally, the TSrPs were washed with DW and stored in desiccator after lyophilization. Surface morphology of TSrPs was observed using field emission scanning electron microscopy (FE-SEM) (JSM 7600 F, JEOL; Tokyo, Japan) and the size was measured using ImageJ software (National Institutes of Health; Stapleton, NE, USA). The morphology and composition of nanoparticles were determined using transmission electron microscopy (TEM) (JEM-ARM200F, JEOL; Tokyo, Japan) and energy dispersive X-ray microanalysis (EDX) at 200 kV. The chemical bonds in the nanoparticles were analyzed via Fourier transform infrared spectroscopy (FT-IR) (Nicolet 6700, Thermo Fisher Scientific; Waltham, MA, USA). The hydrodynamic size and zeta potential of the nanoparticles were determined by using a zetasizer (Zetasizer Nano ZS, Malvern; Worcestershire, UK). Folin–Ciocalteu assay was performed to quantify the total phenol contents in the particles. Briefly, the nanoparticles were dispersed in DW and mixed with the working reagent with mild shaking for 10 min, followed by incubation with 2% sodium carbonate for 1 h. The absorbance was measured at 760 nm via a microplate reader (Varioskan LUX, Thermo Scientific; Waltham, MA, USA). To assess radical scavenging property of the materials, ABTS assay was performed. The particles were sonicated in DW and mixed with 1 mL of ABTS radical solution (7.0 mM ABTS diammonium salt, 2.4 mM potassium persulfate ($K_2S_2O_8$) in PBS). The nanoparticles stored in vacuum were collected different time points after fabrication to investigate time-dependent radical scavenging activity. The absorbance of the solution was determined at 732 nm using microplate reader. To determine the decomposition of H_2O_2, the particles were immersed in DW and mixed with H_2O_2 (100 μM). After 24 h of incubation at RT, the remaining H_2O_2 was measured using a Fluorimetric hydrogen peroxide assay kit according to the manufacturer's instruction (Sigma Aldrich; St. Louis, MO, USA).

2.3. Fabrication and characterization of composite hydrogel

To fabricate G-TSrP, GelMA was dissolved in DPBS (7.5 w/v%) and mixed with the 2-hydroxy-2-methylpropiophenone (0.1 v/v%). Particles with the highest Sr contents, fabricated using a 1 mg/mL TA solution, were dispersed in GelMA solutions with concentrations of 0, 4, and 8 mg/mL. Subsequently, the pre-gel solution (100 μL) was cast into a polytetrafluoroethylene (PTFE) mold (8 mm of diameter, 2 mm of depth, and cylindrical shape). The hydrogels were exposed to UV light (600 mW/cm^2, 2 min) for photo-polymerization. The optical images of hydrogels with different concentrations of TSrPs were obtained by a digital camera. For FE-SEM images, the hydrogels were lyophilized and coated with platinum ion sputter before imaging. The incorporation of nanoparticles in the hydrogels was confirmed by von Kossa staining. Hydrogels were embedded in frozen section compound after immersion in 30% sucrose solution for 1 h, frozen at −70 °C, and cryosectioned into 10 μm using a Cryostat cryocut microtome (Leica Biosystems GmbH, Wetzlar, Germany). The cross-sectioned samples were treated with a 2% silver nitrate solution under a 60 W lamp for 1 h at RT, followed by reaction with 5% sodium thiosulfate for 3 min at RT. To determine swelling ratio of each hydrogel, lyophilized hydrogels were swollen with DPBS for 24 h at RT. The mechanical strength of hydrogels was measured after 24 h of incubation in DPBS at 37 °C and the storage modulus was measured using a rheometer (HR10, TA Instruments; New Castle, DE, USA) under 0.5 N of axial force and 1% of strain. Tensile test was performed using the UniVert mechanical tester (Cell Scale; Waterloo, ON, Canada) to obtain elastic modulus and stress-stain curve of the hydrogels. Hydrogels with same storage modulus were fabricated in rectangular shape and stretched until they were broken. To make same storage modulus of GelMA with G-TSrP, gelation of GelMA was

performed with 10 s of UV irradiation in this experiment. And the OPA assay was performed to investigate the chemical interaction inside the hydrogels. Briefly, each hydrogel was reacted with OPA reagent for 60 s and the fluorescence intensity of the supernatant was measured using microplate reader. To characterize the ROS scavenging effect of TSrPs incorporated hydrogel, ABTS radical scavenging was performed same as mentioned above.

For cell culture, HGM (HDFBs and HaCaT cells), LGM (RAW264.7 cells) and EGM-2 (HUVECs) were used under 5% CO_2 at 37 °C. The HGM and LGM were supplemented with 10% FBS and 1% P/S. We prepared the extract of hydrogels following the standardized protocol (ISO 10993–12). In detail, the hydrogels, with a volume of 100 μL, were placed onto a 24 well plate and subjected to incubation for 24 h at a temperature of 37 °C in 1 mL of a complete cell culturing media. Subsequently, the extracts were collected and subjected to filtration using a 0.22 μm pore size filter in order to remove any hydrogel debris. The cytocompatibility assessment of the hydrogels involved the cultivation of HDFBs, HaCaT cells, and HUVECs with hydrogel extracts for 24 h, with cells cultured in growth medium serving as the control. To culture HUVECs, the extracts were diluted by half. Following this, an MTT assay was conducted by incubating cells with an MTT solution for 1 h at 37 °C, and the resulting MTT formazans were extracted using DMSO. The absorbance of the extracts was measured at 550 nm using microplate reader. For live/dead staining, DPBS containing calcein-AM (1:1000) and ethidium homodimer-1 (1:500) was treated to the cells following 10 min incubation. The samples were then observed using a fluorescent microscope (Eclipse Ti2, Nikon; Tokyo, Japan).

2.4. ROS scavenging activity

The DCFDA assay was used to test the ROS scavenging effect of the hydrogel extract on the HDFBs and RAW264.7 cells. Before the test, the extract from different hydrogels (GelMA group and G-TSrP group) and GelMA extract containing equivalent concentration of TA (TA group) were prepared according to the same amount of TA (20 μM, data not shown). First, DCFDA solution (100 μL, 25 μM) was treated to cells and incubated for 45 min to internalize DCFDA in the cells. Then, the solution was replaced with each hydrogel extract with or without H_2O_2 (1 mM) and incubated for 30 min. Similarly, we carried out the DCFDA assay on RAW264.7 cells using LPS. The cells were incubated with LGM containing LPS (1 μg/mL) for 24 h to induce ROS generation. Subsequently, the medium was replaced with extracts containing LPS (1 μg/mL), and the cells were further incubated for an additional 24 h. The fluorescent intensity of the cultured cells was measured at 485 nm (excitation) and 535 nm (emission), and fluorescence microscope images were captured for analysis. The amount of TA and Sr^{2+} in the medium was measured using Folin-Ciocalteu assay and inductively coupled plasma mass spectrometer (ICP-MS) (iCAP RQ, Thermo Fisher Scientific; Waltham, MA, USA), respectively.

2.5. Evaluation of effect on macrophage polarization

We incubated the cells with extracts containing LPS (1 μg/mL, 24 h) and IL-4 (40 ng/mL, 48 h) to investigate the effect of extracts on M1 and M2 polarization, respectively. The samples were fixed with 4% paraformaldehyde for 20 min at 4 °C and incubated with Alexa 488 phalloidin (1:200) for 2 h at 37 °C for F-actin staining. After mounting with DAPI mounting medium, the stained cells were observed by the fluorescent microscope. The area and aspect ratio of cells were measured using the ImageJ software. For immunofluorescence (IF) staining, LPS and IL-4 treated samples were fixed and incubated with *anti*-iNOS and anti-CD206 antibody solution (1:100 in blocking buffer; 5% of FBS and 0.1% of Tween-20 in PBS), respectively, for 24 h at 4 °C. Then the samples were reacted with anti-rabbit IgG biotin-conjugated secondary antibody (1:100 in blocking buffer) and FITC-conjugated streptavidin tertiary antibody (1:100 in blocking buffer) for 2 h at 37 °C, respectively. The samples were mounted, and the images were captured by the fluorescent microscope. The percentage of iNOS and CD206 positive cells was estimated as the following equation:

$$\frac{N_{ab}}{N_{dapi}} \times 100\ (\%) \quad (1)$$

where N_{ab}, and N_{dapi} were the number of the antibody positive and DAPI signals, respectively.

For RT-qPCR analysis, the samples were lysed with RLT buffer, and the mRNA was purified using a RNeasy Mini Kit (Qiagen, Valencia, USA). After synthesis of cDNA using Maxime RT Premix, RT-qPCR was performed using a StepOnePlus Real-Time PCR System (Applied Biosystems, Foster City, USA) with following procedure: 40 cycles of melting at 95 °C for 15 s and annealing, and extension at 60 °C for 50 s. Comparative threshold cycle (Ct) values were used for comparative gene expression and they were normalized against *glyceraldehyde-3-phosphate dehydrogenase* (*GAPDH*) expression. The sequence of primers used in this experiment is listed in Table S2.

2.6. Evaluation of pro-angiogenic effect

To assess angiogenic gene expression, HDFBs were cultured in extract of GelMA and G-TSrP. The GelMA extract supplemented with equivalent TA concentration of G-TSrP (20 μM, data not shown) was used to evaluate effect of Sr^{2+} on angiogenesis. HDFBs were lysed after 7 days of culture with the extract and RT-qPCR was performed by aforementioned method. The sequence of primers used in this experiment is listed in Table S2. For tubule formation assay, the HUVECs were seeded onto a 48-well culture plate coated with growth factor-reduced Geltrex and cultured with EGM-2 for 12 h. Then the medium was replaced with hydrogel extracts diluted by half and cultured for additional 12 h. For TA group, medium was prepared by adding TA (10 μM) to GelMA extract and diluted by half before use. EBM-2 (supplemented with 10% FBS and 1% P/S) and EGM-2 were used as negative and positive control, respectively. The morphology of the tubules of seeded cells was observed by a phase-contrast microscope (CKX41, Olympus; Tokyo, Japan) and the total length of the branches were quantified by using the ImageJ software. For migration assay, HUVECs were incubated with EGM-2 supplemented with mitomycin C (10 μg/mL) for 2 h and two parallel scratches were made with a yellow pipette tip. Then, each extract was treated for 24 h and the images were observed under a bright field microscope (Eclipse Ti2, Nikon; Tokyo, Japan). The HUVEC-cultured transwell inserts (3 μm pore) were incubated for 24 h in the presence of hydrogels in the lower chamber for transwell migration assay. After removing cells on upper side of the insert using cotton swab, the membranes were fixed with 70% ethanol and stained with crystal violet. The images of migrated cells were taken by the phase-contrast microscope.

2.7. In vivo and in vitro biodegradation of hydrogels

The six-week-old female Balb/c nude mice (Institute for Cancer Research species, Narabiotech; Seoul, Korea) were used for the in vivo implantation of hydrogels into subcutaneous tissue (n = 6). This experiment was approved by the Institutional Animal Care and Use Committee (IACUC) of Hanyang University (approval number: 2022-0081 A). Each mouse was injected with an anesthetic (150 μL) composed of Zoletil (60 mg/kg) and Rompun (20 mg/kg) before surgery. Then, 2 cm incision was made in the middle of the dorsal skin after sterilization with 70% ethanol and the hydrogels were implanted into the subcutaneous tissue. The incised skin was sutured and dressed using Tegaderm™. After two weeks, the mice were sacrificed by CO_2 suffocation and the hydrogel implanted tissues were harvested. The harvested tissues were immersed in 10% formalin for 24 h, followed by dehydration in a series of ethanol solutions (ranging from 70% to 100%) and xylene. Subsequently, the tissues were embedded in paraffin blocks for further processing. The paraffin blocks were sectioned into 10 μm thickness

using a microtome (Leica Biosystems GmbH; Wetzlar, Germany). For hematoxylin and eosin (H&E) staining, the rehydrated samples were treated with hematoxylin for 2 min and eosin for 6 min in RT. After dehydration, the slides were mounted and observed with optical microscopy. For IF staining, the staining was performed with the same protocol as described above. In here, the *anti*-F4/80 antibody and corresponding antibodies for polarization markers (*anti*-iNOS and anti-CD206) were used as primary antibodies. The images of the samples were captured using fluorescence microscope and quantified by ImageJ software. The transwell migration assay and RT-qPCR were performed using RAW264.7 cells through the same protocol as described above. The sequence of primers used in this experiment is listed in Table S2. Degradation of hydrogels was assessed by treating collagenase solution (0.5 CDU/mL in PBS) to GelMA and G-TSrP which have same storage modulus. To make same storage modulus of GelMA with G-TSrP, gelation of GelMA was performed with 10 s of UV irradiation in this experiment. The hydrogels were incubated at 37 °C for 6 h and the images of the hydrogels were taken by the digital camera, and the area of remaining hydrogels was analyzed using ImageJ software. After taking the images, the hydrogels were washed 3 times with DW and lyophilized to determine the mass of the samples. The area and mass loss were normalized by 0 h samples for each group.

2.8. In vivo inflammatory wound healing

To establish the in vivo full-thickness wound healing model, six-week-old female Balb/c mice with 20.0 ± 5.0 g of weight (Orient Bio; Seongnam, Korea) were used (n = 7), and animal management procedures were approved by the IACUC of Ulsan National Institute of Science and Technology (approval number: UNISTIACUC-23-02) under the IACUC guideline. Each mouse was anesthetized with isoflurane during surgery, and a circular biopsy-punched 8 mm full-thickness wound was made on a dorsal region. In here, hydrogels were fabricated in 10 mm diameter and each hydrogel has same storage modulus as described above. The mice without implantation were used as negative control (defect group) and the mice implanted with TA-absorbed hydrogel (Same amount of TA with G-TSrP according to Fig. 2e) was used as TA group. After implantation of the hydrogels, all the mice were injected with LPS (10 μL of 100 μg/mL LPS diluted in PBS) to induce prolonged inflammation for every 3 days. The images of wound were captured via digital camera and wound closure area was analyzed using ImageJ software. The mice were sacrificed by CO_2 suffocation after 3 weeks and the skins were embedded in the paraffine block. H&E and IF staining were performed by the same protocol as described above. For IF staining of cytokeratin, anti-wide spectrum cytokeratin antibody (1:200 in blocking buffer) was used as primary antibody. Wound length, granulation thickness, number of hair follicle and epidermis thickness was analyzed using ImageJ software. To assess the collagen deposition in granulation tissue, the hydrated tissue sections were performed with Masson's trichrome staining according to the manufacturer's protocol. Briefly, the samples were stained sequentially using Weigert's iron hematoxylin solution, followed by Biebrich scarlet acid fuchsin solution, and then aniline blue solution. Finally, the stained samples were mounted for further analysis. Immunohistochemistry (IHC) staining was performed by the same protocol until the primary antibody treatment using anti-COL I antibody (1:200 in blocking buffer) as a primary antibody. Then, the samples were treated with anti-rabbit IgG HRP-conjugated secondary antibody (1:500 in blocking buffer) for 2 h at 37 °C. The intensity of COL I signal was analyzed using ImageJ software. The samples were incubated with DAB substrate solution for 10 min at RT following incubation with hematoxylin solution for 2 min at RT. Also, Sirius red staining was performed using the slides following manufacture's instruction. Briefly, the samples were treated with a Sirius red/Fast green solution after hydration, and they were reacted with extraction buffer. The intensity of the extracted solution was measured at wavelengths 540 nm and 605 nm. The amount of collagen in each section was calculated using the following equation:

$$\frac{(O.D._{540} - (O.D._{605} \times 0.291))}{0.0378} \quad (2)$$

where $O.D._{540}$, and $O.D._{605}$ were the optical density of the solution observed at 540 nm and 605 nm, respectively. The images of the stained samples were obtained by bright-field microscope. IF staining and quantification of α-SMA or CD31 was performed as described above.

2.9. RNA sequencing of macrophages treated with LPS

Prior to treatment of extracts, RAW264.7 cells were cultured in the medium containing LPS (1 μg/mL) for 24 h. Then, the cells were incubated in the extract from different hydrogels (GelMA and G-TSrP group) and GelMA extract containing equivalent concentration of TA (TA group) supplemented with LPS (1 μg/mL) for 24 h. Total RNA was isolated using the column-based kit (QIAGEN RNeasy plus mini kit) according to the manufacturer's instructions. Total RNA sample were sent to Genome Insight (Seoul, Korea) for RNA-Seq. The library was prepared using the TruSeq Stranded mRNA sample preparation kit (Illumina; San Diego, CA, USA) according to the manufacturer's protocol. High-throughput sequencing (2 × 100 bp) was performed on an Illumina NovaSeq 6000 system (Illumina; San Diego, CA, USA). All data analysis and visualization of differentially expressed genes (DEGs) was conducted using R version 4.2.2. Briefly, we preprocessed the raw reads from the sequencer to remove low quality and adapter sequence before analysis and aligned the processed reads to the *Homo sapiens* using "Bowtie2" version 2.5.1. Gene count matrices were summarized using "featureCounts" from Subread version 2.0.4. The reference genome sequence and annotation data of *Homo sapiens* (GRCh38. p14) were downloaded from the NCBI database. Based on the result of that, expression abundance of gene was calculated as FPKM value (Fragments Per Kilobase of exon per Million fragments mapped) per sample. The expression profiles are used to do additional analysis such as DEGs. In groups with different conditions, differentially expressed genes or transcripts can be filtered through statistical hypothesis testing. The cut-off values were |fold change| ≥ 1.5 and p-value <0.05. Heatmap was generated using "pheatmap" version 1.0.12. FPKM values were z-scaled and used as input data for heatmap construction. Volcano plot was generated using "EnhancedVolcano" version 1.16.0 to visualize the results of differential expression analysis. The log2 normalized fold change and -log10 normalized p-value obtained from the comparison plotted as the volcano plot. Functional analysis was performed using "clusterProfiler" version 3.18.1 based on DEGs, which supports statistical analysis and visualization of biological function for genes and their clusters.

2.10. Statistical analysis

All quantitative data were calculated and expressed without preprocessing as mean ± SD with minimum of three independent experiments. GraphPad Prism 7.0 software (La Jolla, CA, USA) was used to perform one or two-way analysis of variance (ANOVA) followed by Tukey's honestly significant difference test for all investigations except those comparing two groups, which were analyzed by Student's t-test. Significances were indicated on all figures and p-values less than 0.05 were considered significant. All the sample sizes (n) were calculated from at least triplicate samples (n ≥ 3). In all figures, all sample sizes and statistical significances were independently denoted in the figure legends.

3. Results and discussion

3.1. One-step fabrication and characterization of metal-phenolic nanoparticles

First, we developed a one-step method to prepare nanoparticles that

allowed for delivery of both TA and Sr^{2+} to a wound. As shown in Fig. 2a, images taken using a SEM and a TEM exhibited bumpy spherical structures with average diameters of 548, 308 and 213 nm for nanoparticles prepared with TA at concentrations of 1, 5 and 10 mg/mL, respectively (Fig. 2b). In the past, self-assembly of polyphenols and metal ions has been utilized for the preparation of nanoparticles due to their strong inter-molecular interactions in short periods of time [33]. However, the need for supporting template materials increases the likelihood of cytotoxicity, and particles composed solely of polyphenols often degrade rapidly at a physiological pH [24,34]. It has been recently developed that use of TA and 10*X* simulated body fluids to induce spontaneous and rapid nanoparticle assembly, mimicking natural mineralization [18]. Here, we modified this method by incorporating Sr^{2+} and excluding unnecessary components, such as Mg^{2+} and K^{+}. One-step nanoparticle formation was achieved within 10 min via supramolecular self-assembly. This may be induced through the LaMer nucleation mechanism; nucleation was evident in the initial stage of the reaction, nuclei growth proceeded through coalescence, and electrostatic interactions between Sr^{2+} and PO_4^{3-} led to the formation of firm organic-inorganic composite nanoparticles with relative homogeneous particle sizes (Fig. S1, Supporting Information) [18,35]. Changes in particle morphology remained almost unaffected irrespective of the TA concentration (Fig. S2, Supporting Information). However, as the quantity of TA increased, the size of the individual particles decreased (Fig. 2b). This response can be attributed to the increase in highly polar TA within the polar aqueous solution; as a concentration of TA rises, the solvent can take control of the growth process, resulting in the formation of smaller particles [36].

We then performed FT-IR analysis (Fig. 2c). The absorption peak at 3000–4000 cm^{-1} in all groups can be attributed primarily to OH stretches in TA [37]. The prominent absorption peaks at 1050 cm^{-1} and 650 cm^{-1} respectively correspond to the PO_4^{3-} and Sr–O peaks. These peaks demonstrate that, with an increase in TA concentration, the bonding between Sr^{2+} and PO_4^{3-} was relatively inhibited, indicating that the negatively charged PO_4^{3-} competes with TA for incorporation. Despite the presence of Na^{+} and Cl^{-} at high concentrations, they were rarely found inside the particles (Fig. S3a, Supporting Information), suggesting that TA favored interactions with divalent over monovalent cations [38]. The mass percentage of strontium and phosphorus in TSrP decreased consistently in response to a higher concentration of TA (Fig. 2d, Fig. S3b, Supporting Information). A Folin-Ciocalteu assay confirmed the increase in total phenol content was proportional to the TA concentration (Fig. 2e). An analysis of the zeta potential showed that, as the concentration of TA increased, the surface charge decreased, suggesting the presence of TA on the surface (Table S1, Supporting Information). The radical-scavenging effect of TA through electron transfer was maintained in TSrPs and proportionally increased with the increase in the concentration of nanoparticles (Fig. 2f) which was also retained for up to 21 days, making long-term storage possible (Fig. S4a, Supporting Information). This implies that TSrP has a strong ROS-scavenging effect, partially through the decomposition of relatively stable H_2O_2 (Fig. S4b, Supporting Information) [39]. Utilizing one-step synthesis with the divalent ion developed in this study, it was possible to achieve homogeneous formation of ROS-scavenging nanoparticles of controlled size and composition.

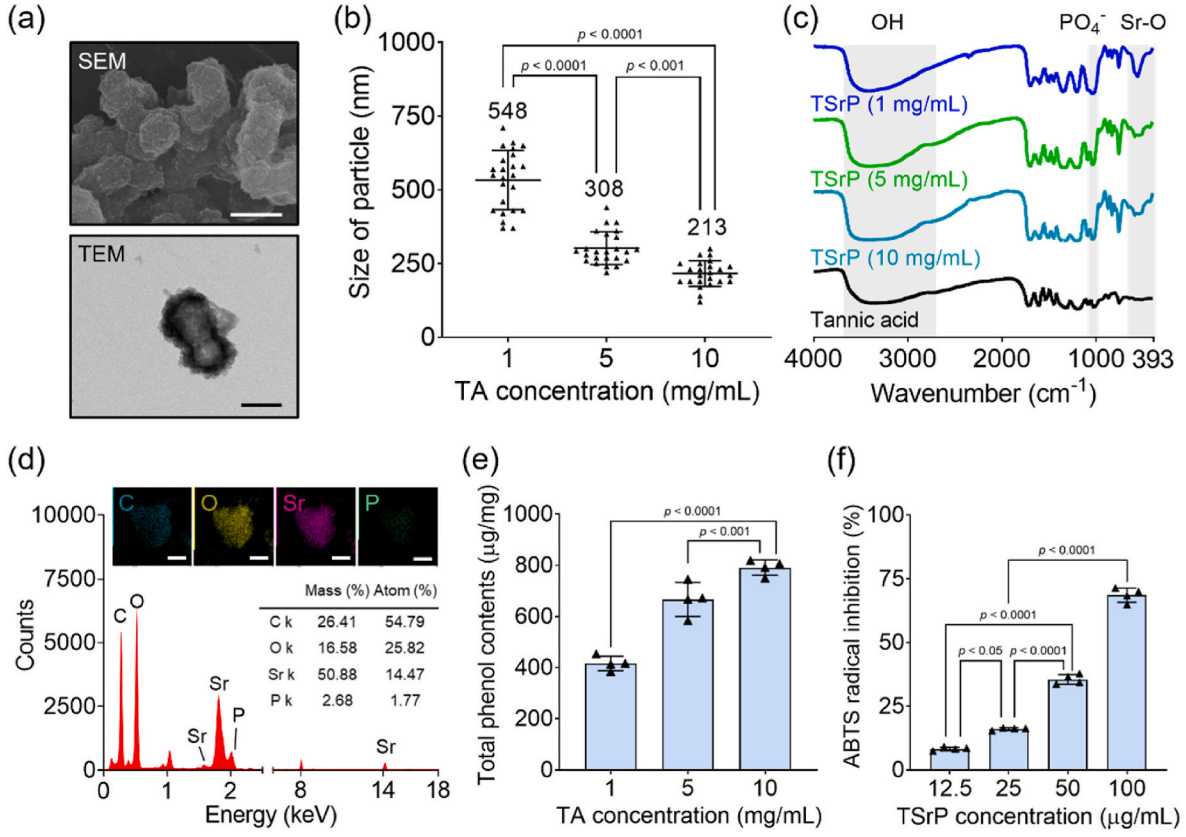

Fig. 2. Fabrication and characterization of TSrP. (a) Scanning electron microscopy (SEM) (top, scale bar: 500 nm) and transmission electron microscopy (bottom, scale bar: 250 nm) images of TSrP fabricated with 1 mg/mL TA. (b) Size distribution of nanoparticles made of different concentrations of TA. (c) Fourier transform infrared spectroscopy spectra of the nanoparticles. (d) Energy dispersive X-ray (EDX) elemental mapping and analysis of the TSrP fabricated with 1 mg/mL TA. Scale bar: 250 nm. (e) Results of a Folin-Ciocalteu assay of total phenol content of TSrPs prepared with different TA concentrations. (f) ABTS radical-scavenging effect of different concentrations of TSrP fabricated with 1 mg/mL TA.

3.2. Physiochemical characterization of TSrP-incorporated GelMA hydrogels

GelMA was obtained through the methacrylation of gelatin, allowing for the formation of photo-crosslinked covalent bonds, which have been widely investigated as composite forms by embedding nanoparticles and other biomaterials for diverse applications in biomedical engineering [40,41]. We incorporated TSrPs into the GelMA solution during the crosslinking reaction, as depicted in Fig. 3a. The resulting hydrogels acquired a brownish-green hue and darkened as the concentration of TSrP increased. SEM images confirmed the presence of embedded nanoparticles and von Kossa staining images of hydrogels indicated the homogenous distribution of nanoparticles inside the hydrogel (Fig. 3b, Fig. S5, Supporting Information). The homogeneity of self-assembled nanoparticles within hydrogels seen in this study highlighted the benefits of using hydrogel-based nanoparticle delivery systems. This approach may overcome the limitations associated with previous direct delivery of self-assembled nanoparticles including restricted local delivery or aggregation [42–44]. The increase in the pore size of the hydrogel (Fig. 3b), along with the greater hydrophilicity resulting from TA deposition, led to augmentation of the swelling ratio through the diffusion of water into the polymer network (Fig. 3c) [45]. Meanwhile, the storage modulus decreased due to the scavenging of free radicals by TSrPs (Fig. 3d). It was investigated that potent antioxidants can scavenge ROS, which is required for the creation of covalent bonds between methacrylate groups [40]. When the hydrogels were prepared with the same storage modulus by reducing the UV irradiation time for GelMA (Fig. S6a, Supporting Information), the Young's modulus of G-TSrP (1.86 ± 0.47) was significantly lower than that of GelMA (3.13 ± 0.57), demonstrating that the incorporation of TSrP produced a hydrogel with both more flexibility and toughness (Fig. 3e, Fig. S6b, Supporting Information). An OPA assay revealed significant reductions in free primary amine groups in G-TSrP compared with GelMA, indicating that the primary amines from lysine-rich gelatin likely formed hydrogen bonds with the hydroxyl groups on the surface of the TSrP (Fig. 3f), confirming previously reported findings [46,47]. G-TSrP also exhibited a dose-dependent ROS-scavenging property due to the presence of TSrP (Fig. 3g). No detrimental effects of G-TSrP on cytocompatibility with various cell types, including fibroblasts, keratinocytes, and endothelial cells, was found when the cells were cultured with hydrogel extracts. (Fig. 3h and i, Fig. S7, Supporting Information).

3.3. Anti-oxidative potential of G-TSrP

As a wound heals, an increase in ROS is essential for the initial clearance of pathogens. However, excessive amounts of ROS can lead to

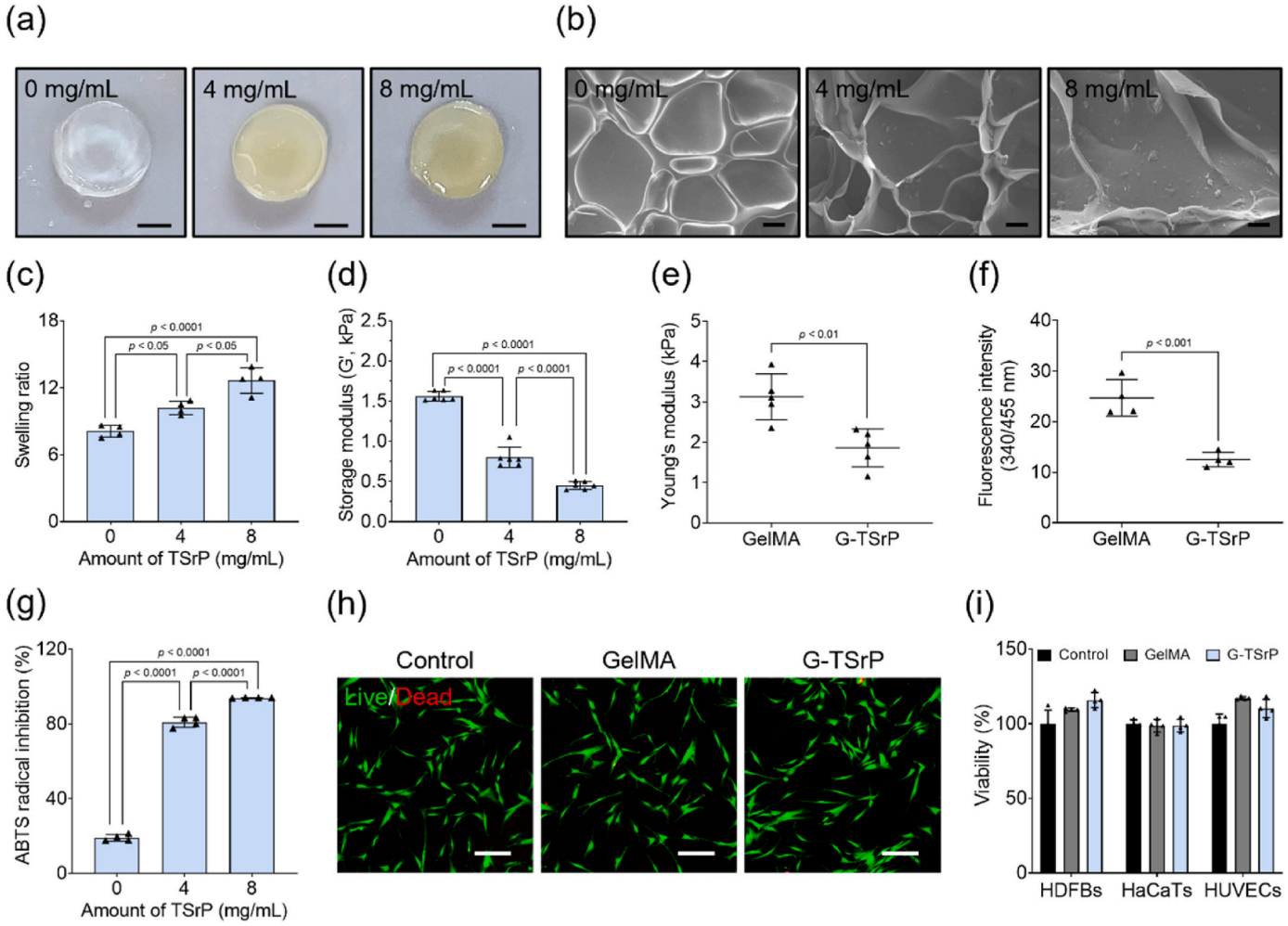

Fig. 3. Characterization and biocompatibility of nanocomposite hydrogels. (a) Optical images of hydrogels with different concentrations of TSrP. Scale bar: 4 mm. (b) SEM images of cross-sectioned hydrogels after lyophilization. Scale bar: 50 μm. (c) Swelling ratio of hydrogels with different concentrations of TSrP and their (d) storage modulus. (e) Young's modulus obtained from tensile test and (f) *o*-phthalaldehyde assay result of GelMA and G-TSrP hydrogels (8 mg/mL TSrP) with the same storage modulus. (g) ABTS radical-scavenging effect of hydrogels with different TSrP concentrations. (h) Representative live/dead staining images of human dermal fibroblasts (HDFBs) (scale bar: 250 μm) and (i) viability of various cell types cultured with hydrogel extracts for 24 h.

an imbalance in immune cells, resulting in the development of chronic wounds [48–50]. Here, we investigated the effect of the components released from the composite hydrogels on removal of oxidative stress. A DCFDA assay revealed a significant reduction in intracellular ROS levels in both fibroblasts and macrophages treated with the G-TSrP extract under H_2O_2-induced oxidative stress (Fig. 4a and b). To imitate the inflammation environment, macrophages challenged with a LPS for 24 h were also exposed to hydrogel extracts in the continuous presence of LPS, and the ROS production was also significantly reduced by extracts of G-TSrP (Fig. 4c). TSrP demonstrated superior ROS-scavenging effects compared with soluble TA at the same concentration (Fig. S8, Supporting Information). Although further investigation is necessary, Sr^{2+} may have increased the expression of anti-oxidative proteins such as superoxide dismutase and glutathione peroxidase, thereby regulating intracellular ROS levels [51,52]. Release profiles of TA and Sr^{2+} from the hydrogel showed that approximately 500 μM of Sr^{2+} and 10 μM of TA were present after 24 h of extraction (Fig. 4d). Previous studies have shown that TA is toxic to fibroblasts at concentrations of 40 μM or higher, while Sr^{2+} displayed toxicity to both fibroblasts and HaCaT cells at 20 mM and higher [53]. The concentration of biologically active TA and Sr^{2+} released from the hydrogel therefore appeared to be within a cytocompatible range.

3.4. Effect of released TA and Sr^{2+} on macrophage polarization

It is crucial to regulate the polarization of M1 macrophages during the early stages of inflammatory process [3]. To achieve this objective, researchers have examined the polarization of macrophages by delivering specific ligands [54–56] or by using external stimuli [57,58] like ultrasound. However, the delivery of ions or soluble components using the hydrogel offers distinct benefits in terms of efficacy, as it overcomes limitations associated with off-target effects or rapid clearance inside the body. Macrophages subjected to LPS treatment were associated with a significant upsurge in the population of inducible iNOS-positive M1 macrophages, levels of which were significantly decreased in the presence of the G-TSrP extracts (Fig. 5a, Fig. S9a, Supporting Information). We then observed a notable increase in cell size in the LPS-treated groups while cells cultured with an extract of G-TSrP exhibited only minimal change (Fig. 5b). iNOS serves as a hallmark of M1 macrophages, playing a critical role in pathogen clearance through nitric oxide generation [59]. M1 macrophages have larger cell areas and less-motile characteristics due to the inhibition of myosin II contraction through a rho-associated protein kinase (ROCK)-independent pathway [60]. Collectively, our results suggest that G-TSrP extracts suppressed M1 polarization of macrophages. To investigate the effect of G-TSrP extract on M2 polarization, we used IL-4. Macrophages treated with IL-4 showed a significant increase in expression of the M2 marker protein CD206, and a further increase was evident in the presence of G-TSrP extract (Fig. 5c, Fig. S9b, Supporting Information). The aspect ratio consistently increased following treatment with IL-4, and a synergistic increase was observed in the presence of G-TSrP extract (Fig. 5d), suggesting M2 polarization of macrophages [60]. The decrease in gene expression of M1 polarization markers (*TNF-α, iNOS* and *IL-1β*) with an increase in M2 polarization markers (*CD163* and *CD206*) in the G-TSrP group further supports the extract's influence on the active regulation of macrophage polarization (Fig. 5e and f). We then compared the down- and up-regulation of M1 and M2 polarization of macrophages treated with G-TSrP extracts and soluble TA in the presence of LPS and IL-4, respectively. We found the G-TSrP group had minimal effect on M1 polarization, while significant up-regulation in the expression of M2

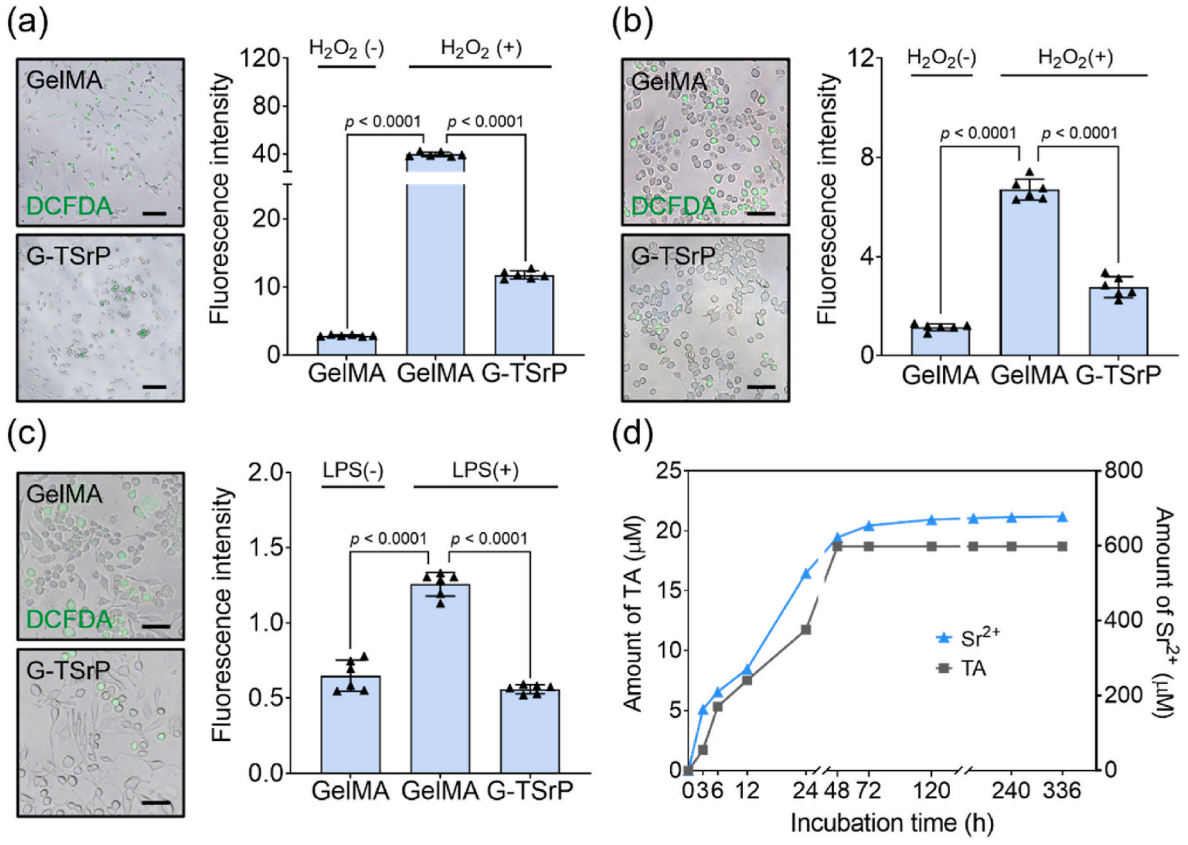

Fig. 4. Intracellular reactive oxygen species (ROS)-scavenging effect of G-TSrP and release profile of TA and Sr^{2+}. 2′,7′-dichlorofluorescein diacetate (DCFDA) assay images and their quantification using (a) HDFBs (scale bar: 100 μm) and (b) RAW264.7 cells (scale bar: 50 μm) treated with different hydrogel extracts and H_2O_2. (c) DCFDA assay images and their quantification using RAW264.7 cells after treatment of hydrogel extracts and lipopolysaccharide (LPS). Scale bar: 50 μm. (d) Release profile of TA and Sr^{2+} from G-TSrP for 14 days.

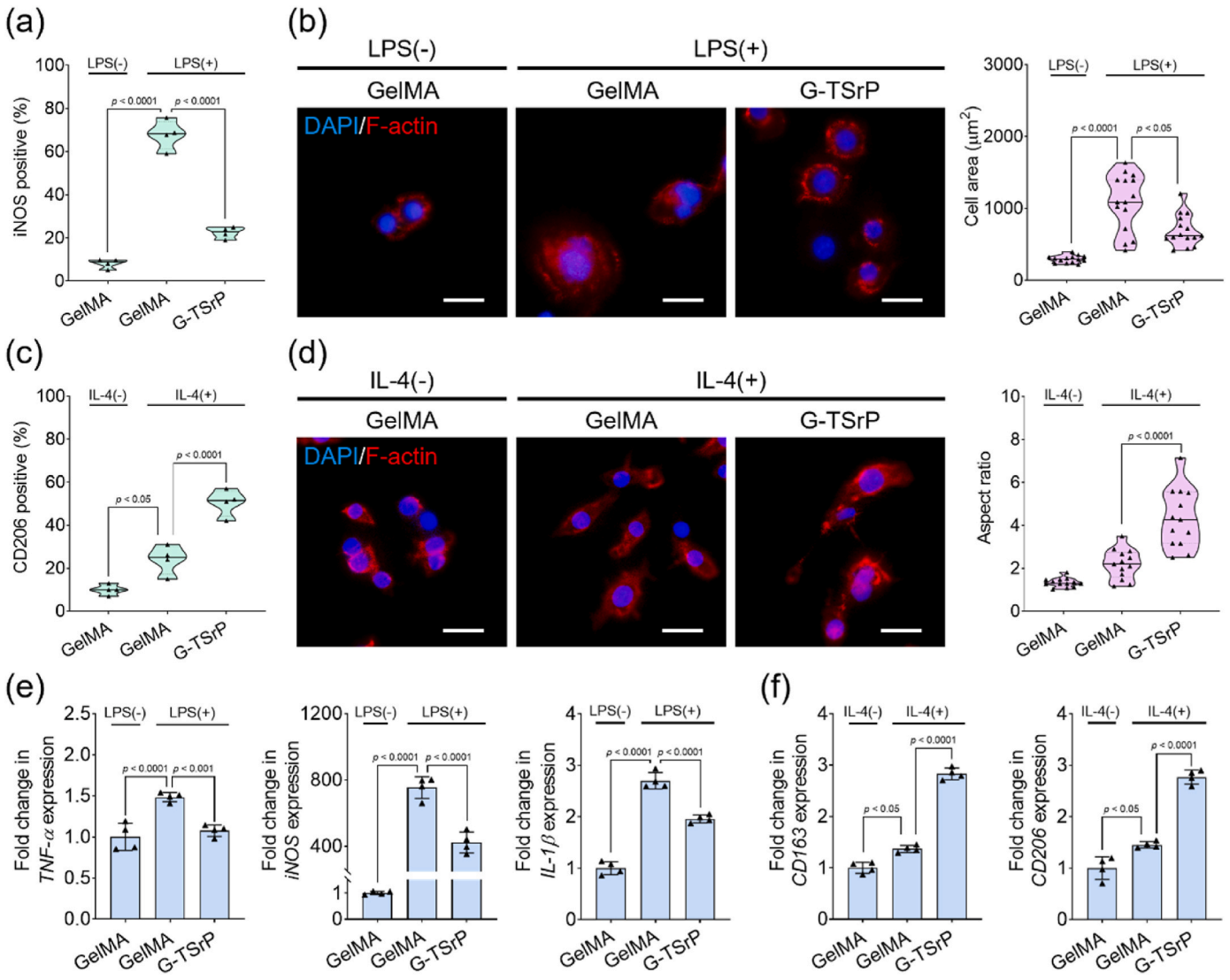

Fig. 5. Modulation of macrophage polarization by G-TSrP. (a) Percentage of iNOS-positive cells from immunofluorescence (IF) images of RAW264.7 cells after treatment with LPS and hydrogel extracts. (b) F-actin staining images of RAW264.7 cells after treatment with LPS and hydrogel extracts, along with measurement of their cell area. Scale bar: 25 μm. (c) Percentage of CD206-positive cells from IF images of RAW264.7 cells after treatment with interleukin (IL)-4 and hydrogel extracts. (d) F-actin staining images of RAW264.7 cells after treatment with IL-4 and hydrogel extracts, along with measurement of their aspect ratio. Scale bar: 25 μm. Relative gene expression of (e) M1 polarization markers and (f) M2 polarization markers of RAW264.7 cells cultured using hydrogel extracts with their induction factors (M1: LPS, M2: IL-4).

polarization marker genes was achieved relative to TA group. (Fig. S10, Supporting Information). The substantial effects of TA on M1 regulation and the influence of Sr^{2+} on M2 polarization demonstrated that G-TSrP has a modulatory effect on macrophage polarization via their coupled synergistic effect.

3.5. *Effects of released TA and Sr^{2+} on angiogenesis and homing of endothelial cells*

We first confirmed the effect of TA on pro-angiogenic growth-factor secretion and expression of remodeling genes by treating an equivalent amount of TA along with an extract of G-TSrP. Results of RT-qPCR analysis showed down-regulation of *vascular endothelial growth factor* (*VEGF*) and *matrix metalloproteinase* (*MMP*)-*2* expression compared with the GelMA extract (Fig. S11, Supporting Information). In addition, TA did not affect tubule formation and migration of endothelial cells relative to the negative control (Fig. S12, Supporting Information). Previous studies have revealed that TA can bind directly to angiogenic factors, inhibiting the function of cytokines or down-regulating expression of gene such as *VEGF* [61]. Additionally, excessive scavenging of ROS by TA can suppress angiogenesis [62]. These results appeared to be consistent with those of previous reports. To address the anti-angiogenic effect of TA, we introduced Sr^{2+}, a biocompatible and potent pro-angiogenic inorganic component [61]. Sr^{2+} not only enhances the proliferation of fibroblasts and endothelial cells, but also increases tubule formation in endothelial cells, along with elevating the expression of angiogenic factors [63,64]. We cultured HDFBs with hydrogel extracts, as HDFBs produce the ECM essential for tissue repair, aiding endothelial cell functions by supplying angiogenic factors such as VEGF proteins, and promoting vessel sprouting via MMP expression [65–67]. RT-qPCR findings revealed that the G-TSrP group induced approximately twice the amount of *VEGF* expression and 1.5-folds more *MMP-2* expression compared with the GelMA group, indicating that the extract had a pro-angiogenic impact (Fig. 6a). The direct pro-angiogenic capacity of the components in the hydrogels was tested using a tubule formation assay (Fig. 6b). Total branching length was maintained, with an extract of G-TSrP showing levels almost similar to those of a positive control containing growth factors. In addition, a scratch assay (Fig. 6c)

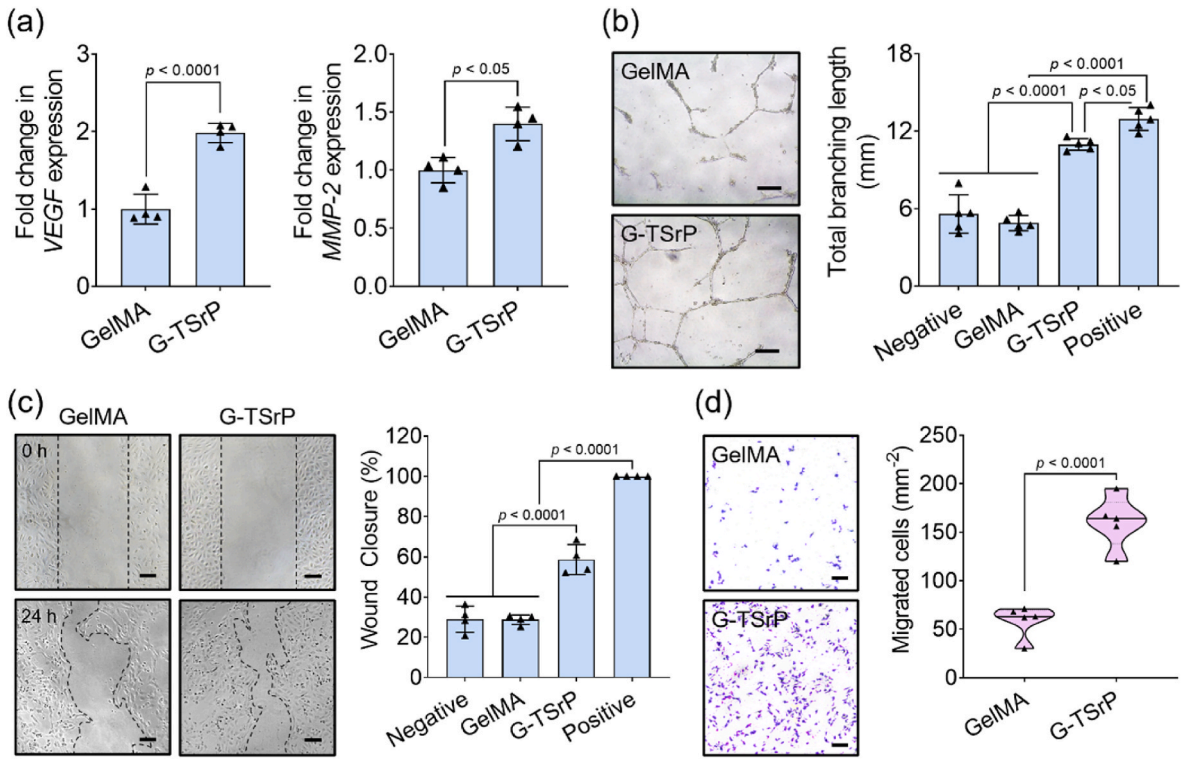

Fig. 6. Effect of G-TSrP on angiogenesis. (a) Relative expression of *vascular endothelial growth factor* (*VEGF*) and *MMP-2* genes of HDFBs cultured with different hydrogel extracts for 7 days. (b) Representative images and the total branching length of human umbilical vein endothelial cells (HUVECs) after treatment of hydrogel extracts. Scale bar: 250 μm. (c) Scratch assay and wound closure after 24 h of incubation with hydrogel extracts. Scale bar: 250 μm. (d) Representative images of transwell migration assay using HUVECs cultured with different hydrogel extracts for 24 h. Scale bar: 125 μm.

produced increased migration of HUVECs in the presence of both TA and Sr^{2+}. A migration assay confirmed the chemo-attractive angiogenic effect of G-TSrP, as indicated by significantly greater migration of endothelial cells (Fig. 6d). Collectively, our results suggest that Sr^{2+} adequately overcomes the somewhat negative angiogenic stimulation of TA, ultimately yielding a pro-angiogenic outcome.

3.6. *Effect of G-TSrP on macrophage homing and degradation of hydrogels*

Based on the role of Sr^{2+} in enhancing the migration of endothelial cells, we hypothesized that a G-TSrP hydrogel may also control infiltration of macrophages. The recruited macrophages would undergo *trans*-polarization into the M2 phenotype, actively regulating enzyme secretion and accelerating the degradation of GelMA hydrogels. To test our hypothesis, we implanted these hydrogels subcutaneously in mice for 14 days. The G-TSrP group demonstrated robust infiltration of cells while the GelMA group displayed only minimal cell infiltration, primarily in the periphery of the implanted hydrogel (Fig. 7a). We observed significant loss of hydrogel volume in the G-TSrP group compared with the GelMA group (Fig. S13a, Supporting Information). We also found significantly higher numbers of migrated cells in G-TSrP compared with GelMA (Fig. S13b, Supporting Information). In addition, the migrated macrophages within the hydrogel were positive for F4/80 at significantly greater numbers (>3 times) in G-TSrP compared with GelMA (Fig. S13c, Supporting Information). Counter-staining of these cells with an M1 marker protein showed that nearly 70% of the recruited macrophages exhibited positive for iNOS (pro-inflammatory M1 phenotype) in the GelMA group, while 5% of the macrophages recruited to the G-TSrP hydrogel displayed the M1 phenotype (Fig. 7b, Fig. S14a, Supporting Information). In contrast, approximately 60% of macrophages in the G-TSrP group displayed CD206 signals (pro-regenerative M2 macrophages) (Fig. 7c, Fig. S14b, Supporting Information). These results suggest that the G-TSrP developed in this study has the potential to enhance cell-mediated degradation of material by actively allowing cell recruitment and immunomodulation. This could be useful for promoting processes such as vascularization and ECM remodeling during cell-mediated tissue regeneration, like normal tissue.

We then attempted to confirm that this phenomenon was a result of cell-mediated biodegradation. Because gelatin-based hydrogels primarily undergo enzymatic degradation, we conducted an in vitro enzymatic degradation test on hydrogels with identical storage moduli (Fig. S6a, Supporting Information) in the presence of collagenase. As shown in Fig. S16a (Supporting Information), all the hydrogels exhibited a similar alteration in their morphology. While the changes in surface area were comparable across the hydrogel samples, G-TSrP demonstrated a slightly accelerated mass loss compared with GelMA (Fig. S16b, Supporting Information). These results indicate that the degradation of hydrogels varied between the in vitro and in vivo experiments. As shown in Fig. 7d, migration of macrophages was significantly enhanced when they were exposed to the G-TSrP. Furthermore, gene expression of MMPs was significantly up-regulated in the same group in the presence of IL-4 (Fig. 7e). A remarkable increase was observed with the G-TSrP extract, compared with the TA group, suggesting that Sr^{2+} plays a significant role in macrophage migration and MMP secretion (Fig. S15, Supporting Information). However, no studies have been conducted on the direct effect of TA and Sr^{2+} on macrophage migration and MMP secretion. Considering previous studies suggest that Sr^{2+} promotes bone-marrow stem-cell migration through the CXCR4 or Erk pathways, we speculated that Sr^{2+} may have facilitated macrophage migration through a similar mechanism [68,69]. Furthermore, M2 macrophages, in contrast to M1 macrophages, exhibit higher motility due to differences in cell contraction, and they engage in mild integrin binding. It is therefore likely that the differentiation of macrophages into M2 as induced by TSrP has contributed to differences in migration [60,70]. It has also been postulated that the increased MMP9 and MMP13 in these induced M2

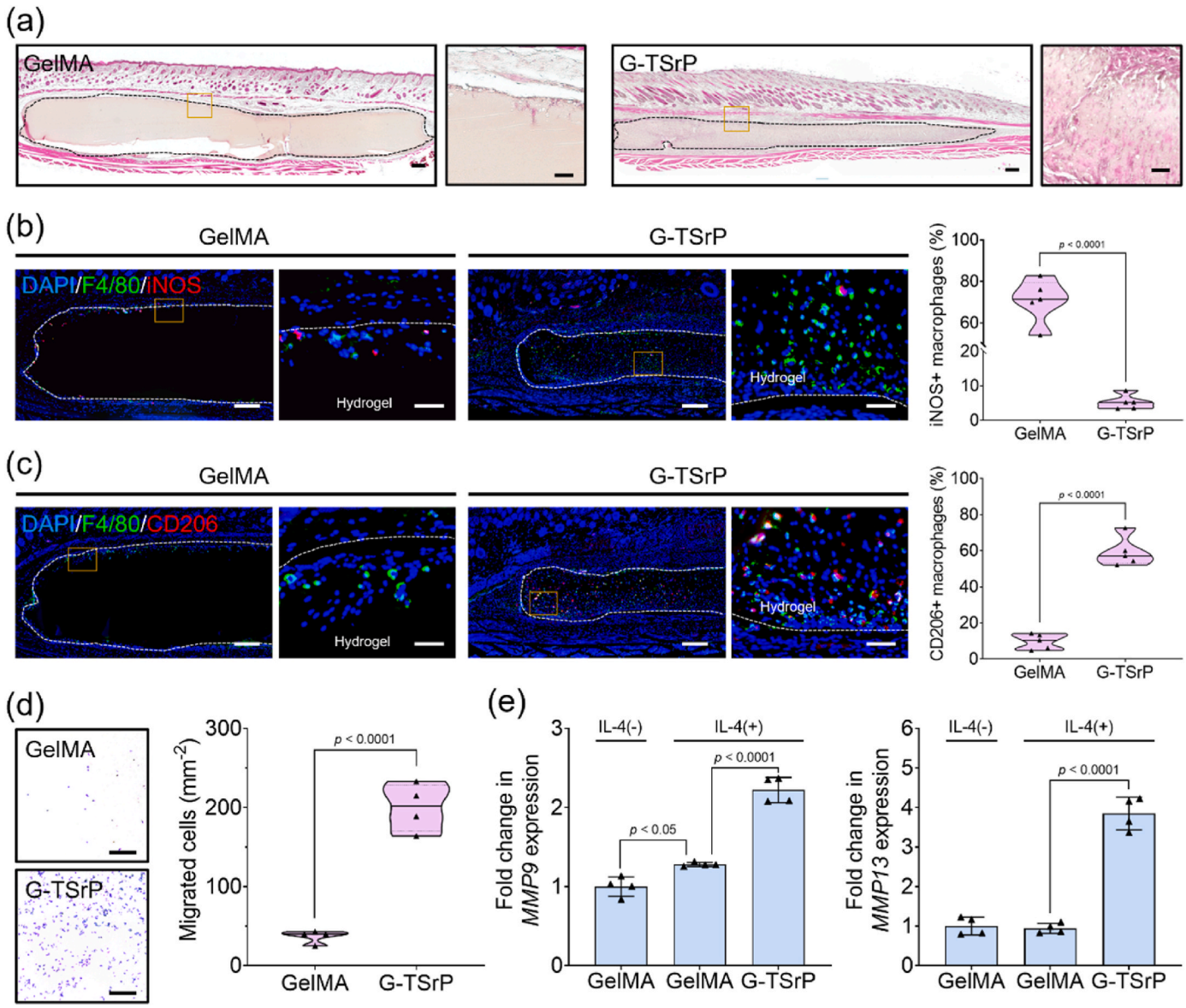

Fig. 7. In vivo and in vitro cell homing and biodegradation of composite hydrogels. (a) Hematoxylin and eosin (H&E) staining images (scale bar: 250 μm) and their magnified images (scale bar: 50 μm) of mouse subcutaneous tissues 14 days after hydrogel implantation. (b) Representative dual IF staining (F4/80 and iNOS) images (scale bar: 250 μm) and their magnified images (scale bar: 50 μm) of mouse subcutaneous tissues 14 days after implantation, along with their quantification. (c) Representative dual IF staining (F4/80 and CD206) images (scale bar: 250 μm) and their magnified images (scale bar: 50 μm) of mouse subcutaneous tissues 14 days after implantation, along with their quantification. (d) Images of migrated RAW264.7 cells cultured with GelMA and G-TSrP hydrogel for 24 h and their quantification. Scale bar: 250 μm. (e) Relative gene expression of *MMP9* and *MMP13* of RAW264.7 cells cultured with IL-4 and each hydrogel extract.

macrophages promote wound healing through ECM remodeling of the hydrogel and tissue [71].

3.7. *In vivo inflammatory wound healing by G-TSrP*

During inflammation, tissue regeneration is often delayed due to excessive persistence of M1 macrophages and inhibited cell migration [6]. To confirm the therapeutic effect of the G-TSrP hydrogel, an excessive-inflammation mouse-wound-healing model was developed in which, following implantation of hydrogels into the wound site, the mouse was treated with LPS every 3 days, as shown in Fig. 8a. The results clearly demonstrated a significant acceleration of the wound-closure process in the group treated with G-TSrP after 6 days of implantation (Fig. 8b and c). When we examined the tissue samples using H&E staining, we observed even more pronounced distinctions in tissue regeneration among the groups (Fig. 8d, Fig. S17a, Supporting Information). The length of the wound was notably shorter, and the thickness of the granulation tissue was significantly greater in the G-TSrP group compared with the other groups (Fig. 8e and f). The rapid repair of open wounds using G-TSrP may have been made possible by positively interacting with the host's immune response to promote tissue regeneration [72]. Promotion of cell infiltration and coordinated hydrogel degradation (Fig. 7) would not only accelerate wound closure but also stimulate the secretion of therapeutic molecules (Sr^{2+} and TA), inducing the formation of granulation tissue. The formation of thick granulation tissue in the G-TSrP group is histologically remarkable. Granulation tissue is formed during the proliferation phase of defect healing, which is characterized by the proliferation of fibroblasts, keratinocytes, and endothelial cells, along with increased production of the ECM [73,74]. In chronic wounds, the accumulation of M1 macrophages reportedly inhibits the formation of granulation tissue. However, an increased population of M2 macrophages can promote granulation

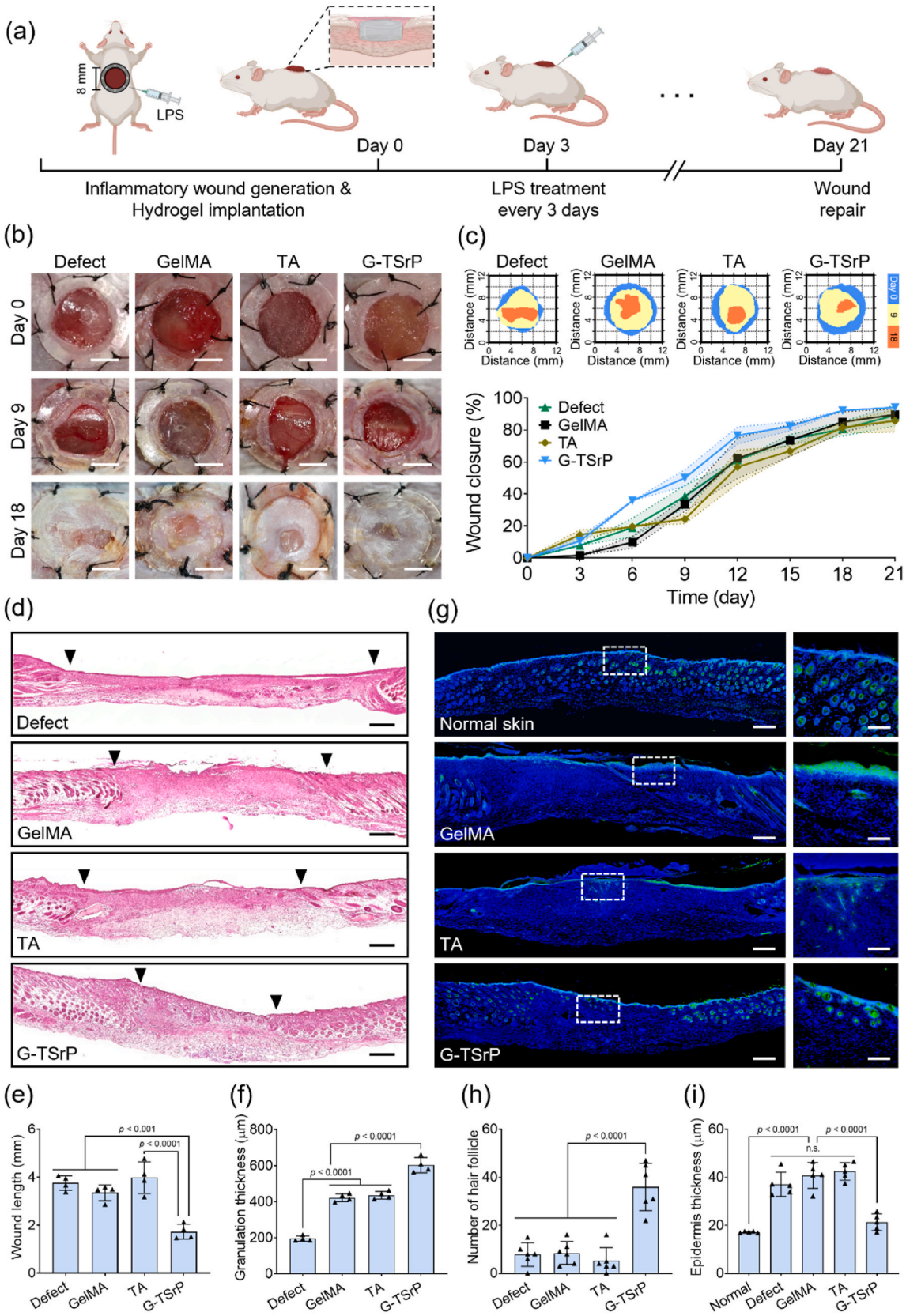

Fig. 8. In vivo inflammatory wound healing. (a) Schematic illustration of the establishment of the inflammatory wound-healing model and the timeline. (b) Representative optical images of wound area after implantation of different hydrogels. Scale bar: 4 mm. (c) Schematic diagram and the quantification of closed wounds. (d) Representative H&E staining images and analysis of the (e) wound length and (f) granulation thickness of wound tissue at day 21. Scale bar: 250 μm. (g) Representative IF staining images (scale bar: 250 μm) and their magnified images (scale bar: 125 μm) of cytokeratin in wounds 21 days after implantation. Analysis of (h) number of hair follicles and (i) epidermis thickness using the IF staining images of cytokeratin.

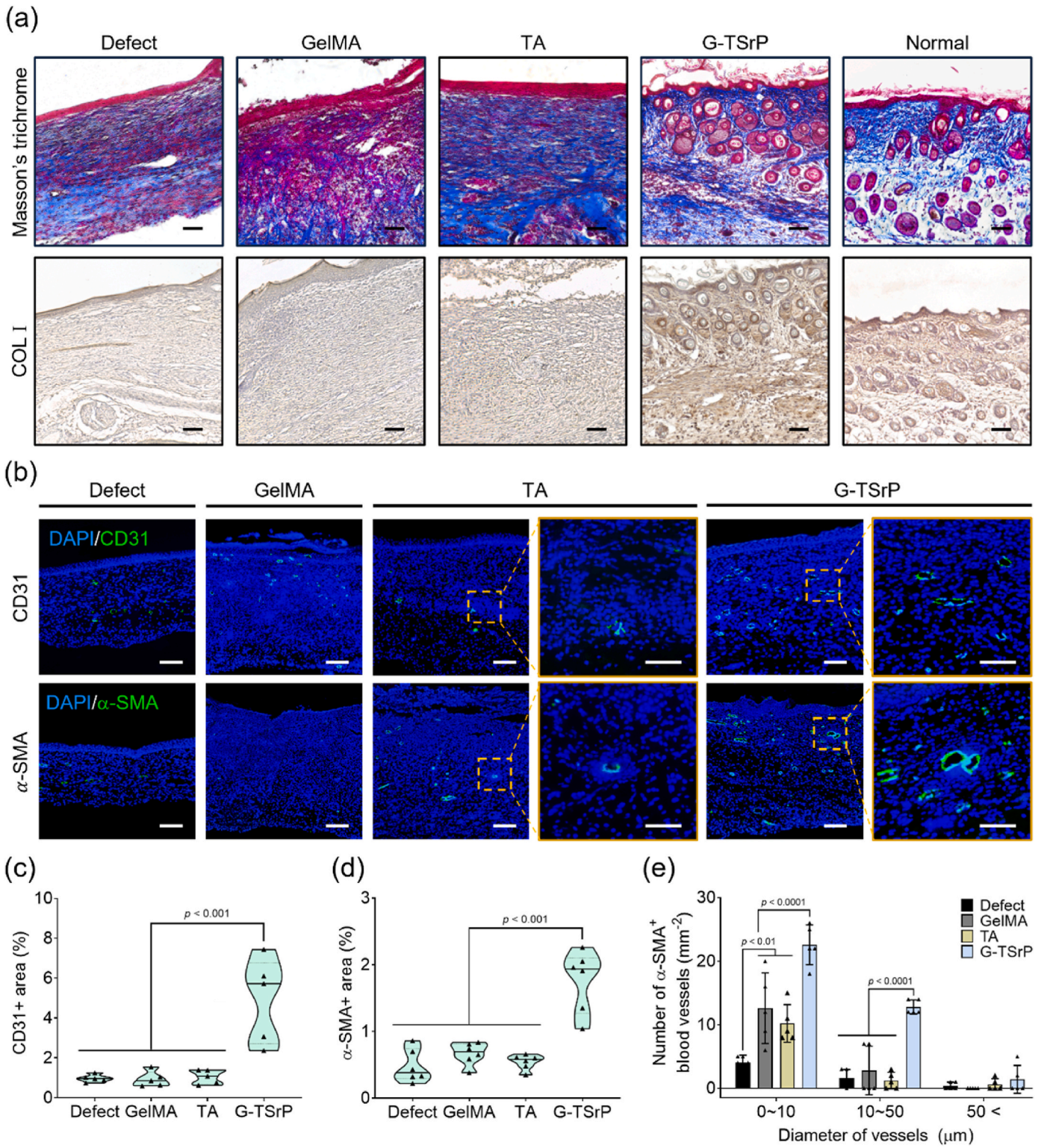

Fig. 9. Tissue remodeling and angiogenesis of inflammatory wound. (a) Masson's trichrome staining and immunohistochemistry (IHC) staining of collagen type I (COL I) images of the wound tissue on day 21. Scale bar: 125 μm. (b) Representative IF images of CD31 and α-SMA (scale bar: 125 μm) of wound tissues on day 21 and their magnified images (scale bar: 30 μm). (c) CD31-positive and (d) α-SMA-positive area analyzed by IF images. (e) Analysis of vessels in wound tissue based on α-SMA-positive vessels in IF images.

tissue by enhancing transforming growth factor-β expression, fibroblast proliferation, and ECM expression [74,75]. Taken together, these observations suggest that immunomodulation by TA and Sr^{2+} promotes wound closure and granulation formation.

IF images of cytokeratin staining provided a clearer depiction of skin-tissue regeneration, with the end product closely resembling normal tissue (Fig. 8g, Fig. S17b, Supporting Information). The G-TSrP group exhibited significantly greater numbers of circular hair follicles compared with the other groups. In fact, the number of hair follicles in the G-TSrP group was five times that observed in the other groups

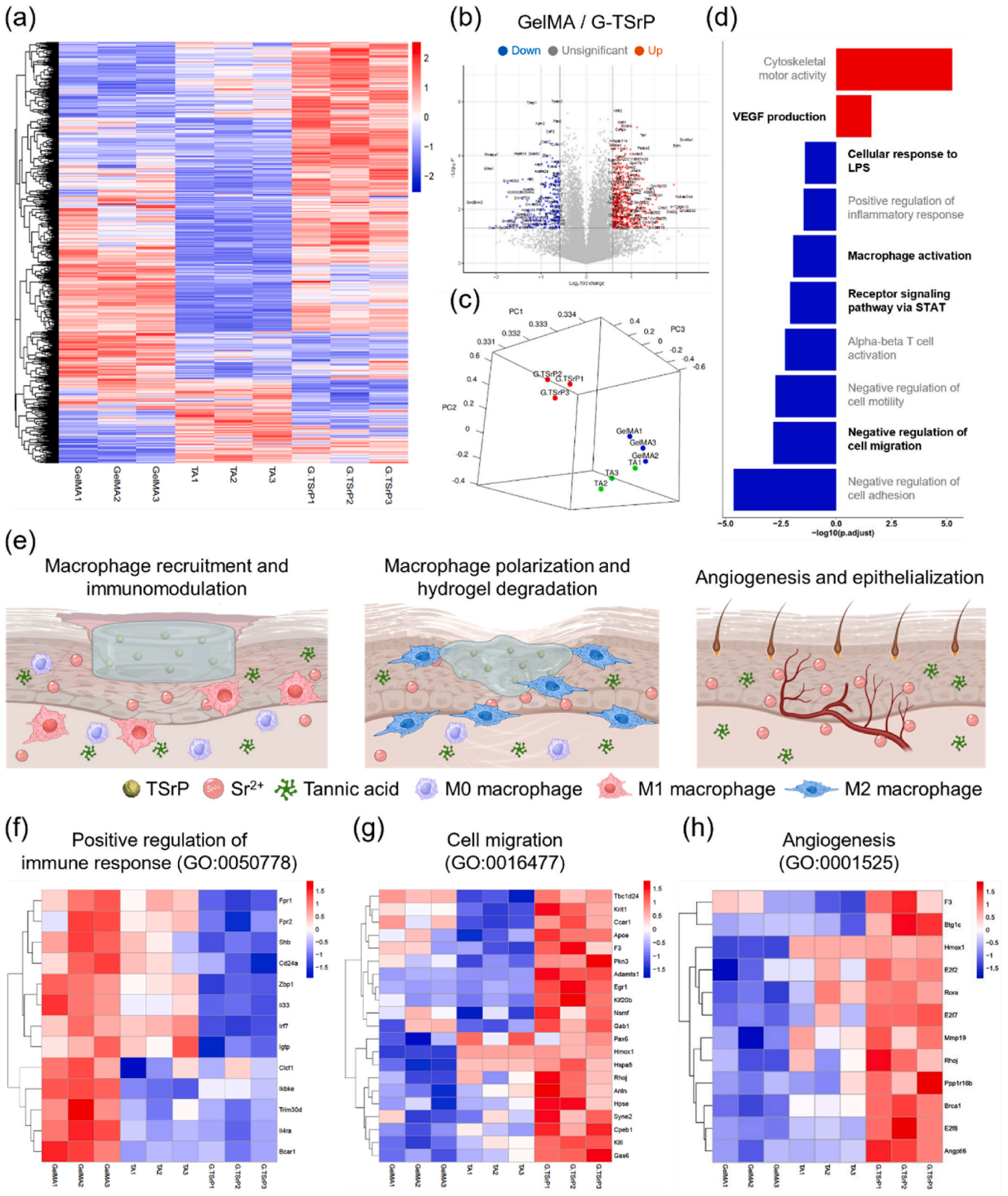

Fig. 10. Genetic analysis of macrophage-mediated inflammatory wound healing. (a) Total heatmap data of RAW264.7 cells after treatment of different hydrogel extracts in the presence of LPS. (b) Volcano plots representing gene expression in the G-TSP group compared with the GelMA group. (c) Principal component analysis (PCA) plot displaying the variances of the genes in macrophages of GelMA, TA and G-TSrP group. (d) Up-regulated and down-regulated gene ontology (GO) analysis. (e) Schematic illustration of the mechanism of macrophage-mediated wound healing process promoted by G-TSrP. GO enrichment analysis of (f) positive regulation of immune response, (g) cell migration, and (h) angiogenesis.

(Fig. 8h). In addition to their fundamental role in hair formation, hair follicles can facilitate wound healing by promoting epithelialization [76]. In the G-TSrP group, the polarized M2 macrophages were likely induced to trigger hair-follicle neogenesis through Wnt signaling in response to growth factors such as fibroblast growth factor-2 and insulin-like growth factor-1, facilitated by the released Sr^{2+} and TA [77]. Moreover, we found that the epidermis thickness associated with the use of G-TSrP was similar to that of normal tissue, potentially demonstrating modulated hyperkeratosis (Fig. 8i). In a chronic wound environment, excessive inflammation leads to continuous secretion of cytokines such as tumor necrosis factor-α (TNF-α), which stimulates keratinocyte proliferation, resulting in thickened epidermis with hyperkeratosis and parakeratosis [78]. However, G-TSrP appears to regulate inflammation, and therefore control the excessive proliferation of keratinocytes.

Regeneration of ECM is essential to preserving the critical function of the skin as a protective barrier [79]. As depicted in Fig. 9a, Masson's trichrome staining and collagen IHC staining in the G-TSrP group revealed a dense connective tissue structure with a pronounced deposition of COL I similar to that of normal skin. Analysis of these histological images further substantiated the significantly greater levels of collagen deposition in the G-TSrP group compared with the other groups (Fig. S18, Supporting Information). Additionally, quantification of collagen levels in each section showed notably elevated collagen deposition in the G-TSrP group (Fig. S19, Supporting Information), suggesting successful ECM remodeling. Based on our findings regarding macrophage recruitment and M2 macrophage polarization (Fig. 7), we concluded that the increased population of M2 macrophages due to G-TSrP helped form this collagen-rich ECM. In addition to collagen deposition, our results show that the G-TSrP group enhanced neo-blood vessel formation with prominent positive staining for endothelial markers, such as α-SMA and CD31, as shown by well-defined circular mature vessel structures (Fig. 9b). The areas occupied by CD31 and α-SMA signals in the G-TSrP group was approximately five times and two times greater, respectively, that those of the other groups (Fig. 9c and d). It is likely that up-regulation of pro-angiogenic signals by Sr^{2+} led to an increased population of M2 macrophages and facilitated the formation of mature vessels positive for α-SMA [23]. Our results also revealed a significant increase in the number of vessels exhibiting arteriolar diameter exceeding 10 μm in the G-TSrP group (Fig. 9e), suggesting that G-TSrP can promote the maturation of recruited endothelial cells, potentially due to its rapid biodegradation and immune modulation based on macrophage polarization.

3.8. Importance in control of macrophages for wound healing via G-TSrP

To elucidate the effects of functional control of G-TSrP over macrophages in the context of inflammatory wound healing, we conducted RNA-seq analysis on macrophages cultured in media supplemented with extracts and TA in the presence of LPS. A hierarchical clustering heatmap representation showed distinctive expression profiles (Fig. 10a). The volcano plot in Fig. 10b showcases the DEGs in the G-TSrP group, indicating a significant up-regulation of 517 genes and a down-regulation of 245 genes compared with GelMA. Also, compared with TA, the G-TSrP group displayed significant differences in DEGs, with 826 up-regulated and 163 down-regulated genes. A principal component analysis (PCA) found the G-TSrP group was clearly separate from both the GelMA and TA groups (Fig. 10c), underscoring the distinct molecular signatures associated with the different treatments and emphasizing the potent impact of G-TSrP on macrophage behavior during inflammatory wound healing. The extract of G-TSrP enhanced macrophage motility in inflammatory conditions and promoted VEGF production through M2 polarization. However, it also down-regulated gene expression associated with pro-inflammation and inhibition of cell migration, such as gene ontologies (GOs) related to cellular response to LPS, STAT receptor signaling, macrophage activation, and pathways leading to decreased cellular motility (Fig. 10d). We postulated a mechanism by which G-TSrP contributes to inflammatory wound-healing through cell migration, immunomodulation, matrix remodeling and the promotion of angiogenesis (Fig. 10e). Upon implantation of G-TSrP, the release of TA and Sr^{2+} stimulates the migration of macrophages toward the implanted area. The macrophages then undergo polarization into M2 macrophages, and subsequently infiltrate the hydrogel. As the hydrogel gradually degrades, the high population of M2 macrophages, in concert with the lingering TA and Sr^{2+} from G-TSrP, actively participates in ECM remodeling and fosters enhanced angiogenesis. Research has shown that the degradation of hydrogel enhanced cellular contact, leading to the integration of stem cells and facilitating overall tissue regeneration [80, 81]. Moreover, an abundance of cell ligands that have the potential to govern the fate of stem cells also have influence on this biological process [82–84]. This culminates in regeneration of the wound, restoring it to a state resembling normal skin tissue. Supporting this proposed wound-healing mechanism of macrophages, a notable down-regulation pattern of GO:0050,778 pertaining to the positive regulation of the immune response was observed in the G-TSrP group, suggesting an immunomodulatory effect of G-TSrP (Fig. 10f). Macrophages influenced by the supplements in G-TSrP promoted cell migration, as seen in Fig. 7, and related changes in gene expression were subsequently evident in the GO:0016,477 category (Fig. 10g). These recruited macrophages facilitated hydrogel degradation through phagocytosis and MMP secretion, which is consistent with an increase in the expression of genes related to metalloendopeptidase activity (GO:0004222), such as *MMP19* (Fig. S20a, Supporting Information). Following hydrogel degradation, M2-polarized macrophages promoted angiogenesis within the empty spaces, forming vascularized tissue. An up-regulation in gene expression associated with angiogenesis was evident in the G-TSrP groups, as shown in Fig. 10h, regarding GO:0001525. Macrophages could then facilitate subsequent tissue remodeling by organization of the ECM (GO:0030,198) (Fig. S20b, Supporting Information). This process includes deposition of collagen and formation of hair follicles, resulting in the regeneration of tissue formation reminiscent of normal tissue. Our findings highlight how G-TSrP accelerates wound healing through macrophage-mediated processes such as matrix remodeling, immunomodulation, cell-homing, and angiogenesis, leading to tissue restoration.

4. Conclusions

We developed a multi-functional nanocomposite hydrogel designed to enhance homing of macrophages and their polarization, ultimately leading to the formation of vascularized tissue in inflamed skin wounds. The nanoparticles integrated into the hydrogel were fabricated using a one-step mineralization technique that leveraged metal-phenolic network formation with TA and Sr^{2+}. These nanoparticles can be seamlessly integrated into a GelMA hydrogel through physical interactions, retaining their unique ability to scavenge ROS. The extracts from these nanocomposite hydrogels not only effectively scavenged intracellular ROS but also promoted M2 polarization while down-regulating M1 polarization of macrophages. Additionally, the extract from the G-TSrP hydrogel exhibited a pro-angiogenic potential, counterbalancing the anti-angiogenic properties of TA. G-TSrP significantly enhanced the homing of various cell types, particularly macrophages and endothelial cells, through chemoattraction and M2 polarization of macrophages. It also helped enhance hydrogel degradation by fostering a cell-mediated biodegradation microenvironment. In an in vivo model of inflammatory wound-healing, we observed accelerated wound closure when using G-TSrP, with the regenerated skin tissue bearing similarities to normal tissue. A genetic analysis of macrophages treated with LPS and hydrogel extracts shed light on the mechanism behind inflammatory wound healing, underscoring the critical role of the composite hydrogel in the homing of macrophages and active modulation of their functions in line with wound healing.

CRediT authorship contribution statement

Hayeon Byun: Writing – review & editing, Writing – original draft, Visualization, Methodology, Investigation, Formal analysis, Data curation, Conceptualization. **Yujin Han:** Writing – review & editing, Writing – original draft, Visualization, Methodology, Investigation, Formal analysis, Data curation. **Eunhyung Kim:** Validation, Methodology, Investigation, Formal analysis, Data curation. **Indong Jun:** Writing – original draft, Visualization, Validation, Investigation, Data curation. **Jinkyu Lee:** Writing – review & editing, Validation. **Hyewoo Jeong:** Methodology, Investigation. **Seung Jae Huh:** Investigation. **Jinmyoung Joo:** Resources, Investigation. **Su Ryon Shin:** Resources. **Heungsoo Shin:** Writing – review & editing, Validation, Supervision, Resources, Project administration, Funding acquisition, Data curation, Conceptualization.

Declaration of competing interest

None.

Acknowledgements

H.B. and Y.H. contributed equally to this work. This work was supported by the National Research Foundation of Korea (NRF) grant funded by the Korea government (MSIT) (No. RS-2023-00207746, RS-2023-00207983) and a grant of the Korea Health Technology R&D Project through the Korea Health Industry Development Institute (KHIDI), funded by the Ministry of Health & Welfare, Republic of Korea (grant number: HI19C075300). The authors specially thank to Minju Kim and Yonghoe Koo at Ulsan National Institute of Science and Technology (Department of Biomedical Engineering, Republic of Korea) for help with the animal experiment. The authors also thank Dr. Giup Jang at Einocle Inc. (Research and Development Center, Republic of Korea) for consultation on RNA sequencing results.

Appendix A. Supplementary data

Supplementary data to this article can be found online at https://doi.org/10.1016/j.bioactmat.2024.02.029.

References

[1] G.C. Gurtner, S. Werner, Y. Barrandon, M.T. Longaker, Wound repair and regeneration, Nature 453 (2008) 314–321, https://doi.org/10.1038/nature07039.
[2] Y.J. Fu, Y.F. Shi, L.Y. Wang, Y.F. Zhao, R.K. Wang, K. Li, S.T. Zhang, X.J. Zha, W. Wang, X. Zhao, W. Yang, All-natural immunomodulatory bioadhesive hydrogel promotes angiogenesis and diabetic wound healing by regulating macrophage heterogeneity, Adv. Sci. 10 (2023) 1–15, https://doi.org/10.1002/advs.202206771.
[3] M. Pasparakis, I. Haase, F.O. Nestle, Mechanisms regulating skin immunity and inflammation, Nat. Rev. Immunol. 14 (2014) 289–301, https://doi.org/10.1038/nri3646.
[4] S.Y. Kim, M.G. Nair, Macrophages in wound healing: activation and plasticity, Immunol. Cell Biol. 97 (2019) 258–267, https://doi.org/10.1111/IMCB.12236.
[5] J. Mao, L. Chen, Z. Cai, S. Qian, Z. Liu, B. Zhao, Y. Zhang, X. Sun, W. Cui, Advanced biomaterials for regulating polarization of macrophages in wound healing, Adv. Funct. Mater. 32 (2022) 1–25, https://doi.org/10.1002/adfm.202111003.
[6] Z. Xu, B. Liang, J. Tian, J. Wu, Anti-inflammation biomaterial platforms for chronic wound healing, Biomater. Sci. 9 (2021) 4388–4409, https://doi.org/10.1039/d1bm00637a.
[7] J.S. Lee, J.S. Lee, M.S. Lee, S. An, K. Yang, K. Lee, H.S. Yang, H. Lee, S.W. Cho, Plant flavonoid-mediated multifunctional surface modification chemistry: catechin coating for enhanced osteogenesis of human stem cells, Chem. Mater. 29 (2017) 4375–4384, https://doi.org/10.1021/acs.chemmater.7b00802.
[8] J. Yeo, J. Lee, S. Yoon, W.J. Kim, Tannic acid-based nanogel as an efficient anti-inflammatory agent, Biomater. Sci. 8 (2020) 1148–1159, https://doi.org/10.1039/c9bm01384a.
[9] A. Sivanantham, D. Pattarayan, R. Bethunaickan, A. Kar, S.K. Mahapatra, R. K. Thimmulappa, R. Palanichamy, S. Rajasekaran, Tannic acid protects against experimental acute lung injury through downregulation of TLR4 and MAPK, J. Cell. Physiol. 234 (2019) 6463–6476, https://doi.org/10.1002/jcp.27383.
[10] D. Li, J. Li, S. Wang, Q. Wang, W. Teng, Dually crosslinked copper-poly(tannic acid) nanoparticles with microenvironment-responsiveness for infected wound treatment, Adv. Healthcare Mater. 12 (2023) 2203063, https://doi.org/10.1002/adhm.202203063.
[11] Y. Li, R. Fu, Z. Duan, C. Zhu, D. Fan, Construction of multifunctional hydrogel based on the tannic acid-metal coating decorated MoS2 dual nanozyme for bacteria-infected wound healing, Bioact. Mater. 9 (2022) 461–474, https://doi.org/10.1016/j.bioactmat.2021.07.023.
[12] K. Wu, M. Fu, Y. Zhao, E. Gerhard, Y. Li, J. Yang, J. Guo, Anti-oxidant anti-inflammatory and antibacterial tannin-crosslinked citrate-based mussel-inspired bioadhesives facilitate scarless wound healing, Bioact. Mater. 20 (2023) 93–110, https://doi.org/10.1016/j.bioactmat.2022.05.017.
[13] Y.W. Kim, T.V. Byzova, Oxidative stress in angiogenesis and vascular disease, Blood 123 (2014) 625–631, https://doi.org/10.1182/blood-2013-09-512749.
[14] G. Rajesh, S. Harshala, G. Dhananjay, A. Jadhav, G. Vikram, Effect of hydroxyl substitution of flavone on angiogenesis and free radical scavenging activities: a structure-activity relationship studies using computational tools, Eur. J. Pharmaceut. Sci. 39 (2010) 37–44, https://doi.org/10.1016/j.ejps.2009.10.008.
[15] E. Hatami, P.K. B Nagesh, M. Sikander, A. Dhasmana, S.C. Chauhan, M. Jaggi, M. M. Yallapu, Tannic acid exhibits antiangiogenesis activity in nonsmall-cell lung cancer cells, ACS Omega 7 (2022) 23939–23949, https://doi.org/10.1021/acsomega.2c02727.
[16] V. Mouriño, J.P. Cattalini, A.R. Boccaccini, Metallic ions as therapeutic agents in tissue engineering scaffolds: an overview of their biological applications and strategies for new developments, J. R. Soc. Interface 9 (2012) 401–419, https://doi.org/10.1098/rsif.2011.0611.
[17] A. Bhattacharyya, M.R. Khatun, S. Narmatha, R. Nagarajan, I. Noh, Modulation of 3D bioprintability in polysaccharide bioink by bioglass nanoparticles and multiple metal ions for tissue engineering, Tissue Eng Regen Med (2023), https://doi.org/10.1007/s13770-023-00605-1.
[18] H. Byun, G.N. Jang, M.-H. Hong, J. Yeo, H. Shin, W.J. Kim, H. Shin, Biomimetic anti-inflammatory and osteogenic nanoparticles self-assembled with mineral ions and tannic acid for tissue engineering, Nano Converg 9 (2022) 47, https://doi.org/10.1186/s40580-022-00338-2.
[19] A.M. Brokesh, A.K. Gaharwar, Inorganic biomaterials for regenerative medicine, ACS Appl. Mater. Interfaces 12 (2020) 5319–5344, https://doi.org/10.1021/acsami.9b17801.
[20] T. Mehrabi, A.S. Mesgar, Z. Mohammadi, Bioactive glasses: a promising therapeutic ion release strategy for enhancing wound healing, ACS Biomater. Sci. Eng. 6 (2020) 5399–5430, https://doi.org/10.1021/acsbiomaterials.0c00528.
[21] Y.W. Chen, T. Feng, G.Q. Shi, Y.L. Ding, X.X. Yu, X.H. Zhang, Z.B. Zhang, C.X. Wan, Interaction of endothelial cells with biodegradable strontium-doped calcium polyphosphate for bone tissue engineering, Appl. Surf. Sci. 255 (2008) 331–335, https://doi.org/10.1016/j.apsusc.2008.06.154.
[22] W. Lu, C. Zhou, Y. Ma, J. Li, J. Jiang, Y. Chen, L. Dong, F. He, Improved osseointegration of strontium-modified titanium implants by regulating angiogenesis and macrophage polarization, Biomater. Sci. 10 (2022) 2198–2214, https://doi.org/10.1039/d1bm01488a.
[23] F. Zhao, B. Lei, X. Li, Y. Mo, R. Wang, D. Chen, X. Chen, Promoting in vivo early angiogenesis with sub-micrometer strontium-contained bioactive microspheres through modulating macrophage phenotypes, Biomaterials 178 (2018) 36–47, https://doi.org/10.1016/j.biomaterials.2018.06.004.
[24] X. Gao, Q. Wang, L. Ren, P. Gong, M. He, W. Tian, W. Zhao, Metal-phenolic networks as a novel filler to advance multi-functional immunomodulatory biocomposites, Chem. Eng. J. 426 (2021) 131825, https://doi.org/10.1016/j.cej.2021.131825.
[25] Y. Liang, J. He, B. Guo, Functional hydrogels as wound dressing to enhance wound healing, ACS Nano 15 (2021) 12687–12722, https://doi.org/10.1021/acsnano.1c04206.
[26] Q. Li, F. Lu, G. Zhou, K. Yu, B. Lu, Y. Xiao, F. Dai, D. Wu, G. Lan, Silver inlaid with gold nanoparticle/chitosan wound dressing enhances antibacterial activity and porosity, and promotes wound healing, Biomacromolecules 18 (2017) 3766–3775, https://doi.org/10.1021/acs.biomac.7b01180.
[27] Y.J. Lin, G.H. Lee, C.W. Chou, Y.P. Chen, T.H. Wu, H.R. Lin, Stimulation of wound healing by PU/hydrogel composites containing fibroblast growth factor-2, J. Mater. Chem. B 3 (2015) 1931–1941, https://doi.org/10.1039/c4tb01638f.
[28] X. Li, S. Chen, B. Zhang, M. Li, K. Diao, Z. Zhang, J. Li, Y. Xu, X. Wang, H. Chen, In situ injectable nano-composite hydrogel composed of curcumin, N,O-carboxymethyl chitosan and oxidized alginate for wound healing application, Int. J. Pharm. 437 (2012) 110–119, https://doi.org/10.1016/j.ijpharm.2012.08.001.
[29] D.R. Griffin, M.M. Archang, C.H. Kuan, W.M. Weaver, J.S. Weinstein, A.C. Feng, A. Ruccia, E. Sideris, V. Ragkousis, J. Koh, M.V. Plikus, D. Di Carlo, T. Segura, P. O. Scumpia, Activating an adaptive immune response from a hydrogel scaffold imparts regenerative wound healing, Nat. Mater. 20 (2021) 560–569, https://doi.org/10.1038/s41563-020-00844-w.
[30] D. Zhang, Q. Chen, Y. Bi, H. Zhang, M. Chen, J. Wan, C. Shi, W. Zhang, J. Zhang, Z. Qiao, J. Li, S. Chen, R. Liu, Bio-inspired poly-DL-serine materials resist the foreign-body response, Nat. Commun. 12 (2021), https://doi.org/10.1038/s41467-021-25581-9.
[31] X. Zhang, Y. Li, Z. Ma, D. He, H. Li, Modulating degradation of sodium alginate/bioglass hydrogel for improving tissue infiltration and promoting wound healing, Bioact. Mater. 6 (2021) 3692–3704, https://doi.org/10.1016/j.bioactmat.2021.03.038.
[32] C.M. Madl, L.M. Katz, S.C. Heilshorn, Tuning bulk hydrogel degradation by simultaneous control of proteolytic cleavage kinetics and hydrogel network architecture, ACS Macro Lett. 7 (2018) 1302–1307, https://doi.org/10.1021/acsmacrolett.8b00664.

[33] M.A. Rahim, S.L. Kristufek, S. Pan, J.J. Richardson, F. Caruso, Phenolic building blocks for the assembly of functional materials, Angew. Chem. Int. Ed. 58 (2019) 1904–1927, https://doi.org/10.1002/anie.201807804.
[34] M.A. Rahim, H. Ejima, K.L. Cho, K. Kempe, M. Müllner, J.P. Best, F. Caruso, Coordination-driven multistep assembly of metal-polyphenol films and capsules, Chem. Mater. 26 (2014) 1645–1653, https://doi.org/10.1021/cm403903m.
[35] N.T.K. Thanh, N. Maclean, S. Mahiddine, Mechanisms of nucleation and growth of nanoparticles in solution, Chem. Rev. 114 (2014) 7610–7630, https://doi.org/10.1021/cr400544s.
[36] M.H. Hussain, N. Fitrah, A. Bakar, A.N. Mustapa, K. Low, N.H. Othman, F. Adam, Synthesis of various size gold nanoparticles by chemical reduction method with different solvent polarity, Nanoscale Res. Lett. 15 (2020) 140–150.
[37] Y. Peng, P. Wu, H.W. Siesler, Two-dimensional/ATR infrared correlation spectroscopic study on water diffusion in a poly(ε-caprolactone) matrix, Biomacromolecules 4 (2003) 1041–1044, https://doi.org/10.1021/bm0340624.
[38] G. Yun, J.J. Richardson, M. Biviano, F. Caruso, Tuning the mechanical behavior of metal-phenolic networks through building block composition, ACS Appl. Mater. Interfaces 11 (2019) 6404–6410, https://doi.org/10.1021/acsami.8b19988.
[39] Z. Chen, J. Duan, Y. Diao, Y. Chen, X. Liang, H. Li, Y. Miao, Q. Gao, L. Gui, X. Wang, J. Yang, Y. Li, ROS-responsive capsules engineered from EGCG-Zinc networks improve therapeutic angiogenesis in mouse limb ischemia, Bioact. Mater. 6 (2021) 1–11, https://doi.org/10.1016/j.bioactmat.2020.07.013.
[40] M.A. Sakr, K. Sakthivel, T. Hossain, S.R. Shin, S. Siddiqua, J. Kim, K. Kim, Recent trends in gelatin methacryloyl nanocomposite hydrogels for tissue engineering, J. Biomed. Mater. Res. 110 (2022) 708–724, https://doi.org/10.1002/jbm.a.37310.
[41] P. Thoniyot, M.J. Tan, A.A. Karim, D.J. Young, X.J. Loh, Nanoparticle–hydrogel composites: concept, design, and applications of these promising, multi-functional materials, Adv. Sci. 2 (2015) 1–13, https://doi.org/10.1002/advs.201400010.
[42] H. Byun, G.N. Jang, H. Jeong, J. Lee, S.J. Huh, S. Lee, E. Kim, H. Shin, Development of a composite hydrogel incorporating anti-inflammatory and osteoinductive nanoparticles for effective bone regeneration, Biomater. Res. 27 (2023), https://doi.org/10.1186/s40824-023-00473-9.
[43] S. Lee, J. Yoo, G. Bae, R. Thangam, J. Heo, J.Y. Park, H. Choi, C. Kim, J. An, J. Kim, K.R. Mun, S. Shin, K. Zhang, P. Zhao, Y. Kim, N. Kang, S.-B. Han, D. Kim, J. Yoon, M. Kang, J. Kim, L. Yang, S. Karamikamkar, J. Kim, Y. Zhu, A.H. Najafabadi, G. Song, D.-H. Kim, K.-B. Lee, S.J. Oh, H.-D. Jung, H.-C. Song, W.Y. Jang, L. Bian, Z. Chu, J. Yoon, J.S. Kim, Y.S. Zhang, Y. Kim, H.S. Jang, S. Kim, H. Kang, Photonic control of ligand nanospacing in self-assembly regulates stem cell fate, Bioact. Mater. 34 (2024) 164–180, https://doi.org/10.1016/j.bioactmat.2023.12.011.
[44] Y. Kim, H.J. Jung, Y. Lee, S. Koo, R. Thangam, W.Y. Jang, S.Y. Kim, S. Park, S. Lee, G. Bae, K.D. Patel, Q. Wei, K.B. Lee, R. Paulmurugan, W.K. Jeong, T. Hyeon, D. Kim, H. Kang, Manipulating nanoparticle aggregates regulates receptor-ligand binding in macrophages, J. Am. Chem. Soc. 144 (2022) 5769–5783, https://doi.org/10.1021/jacs.1c08861.
[45] R. Foudazi, R. Zowada, I. Manas-Zloczower, D.L. Feke, Porous hydrogels: present challenges and future opportunities, Langmuir 39 (2023) 2092–2111, https://doi.org/10.1021/acs.langmuir.2c02253.
[46] C. Xu, W. Lee, G. Dai, Y. Hong, Highly elastic biodegradable single-network hydrogel for cell printing, ACS Appl. Mater. Interfaces 10 (2018) 9969–9979, https://doi.org/10.1021/acsami.8b01294.
[47] C.N. Grover, J.H. Gwynne, N. Pugh, S. Hamaia, R.W. Farndale, S.M. Best, R. E. Cameron, Crosslinking and composition influence the surface properties, mechanical stiffness and cell reactivity of collagen-based films, Acta Biomater. 8 (2012) 3080–3090, https://doi.org/10.1016/j.actbio.2012.05.006.
[48] M. Canton, R. Sánchez-Rodríguez, I. Spera, F.C. Venegas, M. Favia, A. Viola, A. Castegna, Reactive oxygen species in macrophages: sources and targets, Front. Immunol. 12 (2021), https://doi.org/10.3389/fimmu.2021.734229.
[49] Y.-W. Kim, T. V Byzova, Oxidative Stress in Angiogenesis and Vascular Disease, 2014, https://doi.org/10.1182/blood.
[50] Y. Ye, H. Zhong, S. Huang, W. Lai, Y. Huang, C. Sun, Y. Zhang, S. Zheng, Reactive oxygen species scavenging hydrogel regulates stem cell behavior and promotes bone healing in osteoporosis, Tissue Eng Regen Med 20 (2023) 981–992, https://doi.org/10.1007/s13770-023-00561-w.
[51] I.H. El-Sayed, M. Lotfy, O.A.Y. El-Khawaga, W.A. Nasif, M. El-Shahat, Prominent free radicals scavenging activity of tannic acid in lead-induced oxidative stress in experimental mice, Toxicol. Ind. Health 22 (2006) 157–163, https://doi.org/10.1191/0748233706th256oa.
[52] X. Shen, K. Fang, K.H. Ru Yie, Z. Zhou, Y. Shen, S. Wu, Y. Zhu, Z. Deng, P. Ma, J. Ma, J. Liu, High proportion strontium-doped micro-arc oxidation coatings enhance early osseointegration of titanium in osteoporosis by anti-oxidative stress pathway, Bioact. Mater. 10 (2022) 405–419, https://doi.org/10.1016/j.bioactmat.2021.08.031.
[53] R.G. Daré, C.V. Nakamura, V.F. Ximenes, S.O.S. Lautenschlager, Tannic acid, a promising anti-photoaging agent: evidences of its antioxidant and anti-wrinkle potentials, and its ability to prevent photodamage and MMP-1 expression in L929 fibroblasts exposed to UVB, Free Radic. Biol. Med. 160 (2020) 342–355, https://doi.org/10.1016/j.freeradbiomed.2020.08.019.
[54] S. Min, Y.S. Jeon, H. Choi, C. Khatua, N. Li, G. Bae, H.J. Jung, Y. Kim, H. Hong, J. Shin, M.J. Ko, H.S. Ko, T. Kim, J.H. Moon, J.J. Song, V.P. Dravid, Y.K. Kim, H. Kang, Large and externally positioned ligand-coated nanopatches facilitate the adhesion-dependent regenerative polarization of host macrophages, Nano Lett. 20 (2020) 7272–7280, https://doi.org/10.1021/acs.nanolett.0c02655.
[55] X. Huang, L. Wang, H. Guo, W. Zhang, Macrophage membrane-coated nanovesicles for dual-targeted drug delivery to inhibit tumor and induce macrophage polarization, Bioact. Mater. 23 (2023) 69–79, https://doi.org/10.1016/j.bioactmat.2022.09.027.
[56] Y. Kim, T.M. Koo, R. Thangam, M.S. Kim, W.Y. Jang, N. Kang, S. Min, S.Y. Kim, L. Yang, H. Hong, H.J. Jung, E.K. Koh, K.D. Patel, S. Lee, H.E. Fu, Y.S. Jeon, B. C. Park, S.Y. Kim, S. Park, J. Lee, L. Gu, D.H. Kim, T.H. Kim, K.B. Lee, W.K. Jeong, R. Paulmurugan, Y.K. Kim, H. Kang, Submolecular ligand size and spacing for cell adhesion, Adv. Mater. 34 (2022), https://doi.org/10.1002/adma.202110340.
[57] F. Zhang, M. Lv, S. Wang, M. Li, Y. Wang, C. Hu, W. Hu, X. Wang, X. Wang, Z. Liu, Z. Fan, J. Du, Y. Sun, Ultrasound-triggered biomimetic ultrashort peptide nanofiber hydrogels promote bone regeneration by modulating macrophage and the osteogenic immune microenvironment, Bioact. Mater. 31 (2024) 231–246, https://doi.org/10.1016/j.bioactmat.2023.08.008.
[58] Q. Song, D. Wang, H. Li, Z. Wang, S. Sun, Z. Wang, Y. Liu, S. Lin, G. Li, S. Zhang, P. Zhang, Dual-response of multi-functional microsphere system to ultrasound and microenvironment for enhanced bone defect treatment, Bioact. Mater. 32 (2024) 304–318, https://doi.org/10.1016/j.bioactmat.2023.10.007.
[59] G. Lu, R. Zhang, S. Geng, L. Peng, P. Jayaraman, C. Chen, F. Xu, J. Yang, Q. Li, H. Zheng, K. Shen, J. Wang, X. Liu, W. Wang, Z. Zheng, C.F. Qi, C. Si, J.C. He, K. Liu, S.A. Lira, A.G. Sikora, L. Li, H. Xiong, Myeloid cell-derived inducible nitric oxide synthase suppresses M1 macrophage polarization, Nat. Commun. 6 (2015) 1–14, https://doi.org/10.1038/ncomms7676.
[60] L.E. Hind, E.B. Lurier, M. Dembo, K.L. Spiller, D.A. Hammer, Effect of M1–M2 polarization on the motility and traction stresses of primary human macrophages, Cell. Mol. Bioeng. 9 (2016) 455–465, https://doi.org/10.1007/s12195-016-0435-x.
[61] E. Hatami, P.K. B Nagesh, M. Sikander, A. Dhasmana, S.C. Chauhan, M. Jaggi, M. M. Yallapu, Tannic acid exhibits antiangiogenesis activity in nonsmall-cell lung cancer cells, ACS Omega 7 (2022) 23939–23949, https://doi.org/10.1021/acsomega.2c02727.
[62] Y.W. Kim, T.V. Byzova, Oxidative stress in angiogenesis and vascular disease, Blood 123 (2014) 625–631, https://doi.org/10.1182/blood-2013-09-512749.
[63] M. Xing, Y. Jiang, W. Bi, L. Gao, Y.L. Zhou, S. Le Rao, L.L. Ma, Z.W. Zhang, H. T. Yang, J. Chang, Strontium ions protect hearts against myocardial ischemia/reperfusion injury, Sci. Adv. 7 (2021), https://doi.org/10.1126/sciadv.abe0726.
[64] M. Šalandová, I.A.J. van Hengel, I. Apachitei, A.A. Zadpoor, B.C.J. van der Eerden, L.E. Fratila-Apachitei, Inorganic agents for enhanced angiogenesis of orthopedic biomaterials, Adv. Healthcare Mater. 10 (2021) 2002254, https://doi.org/10.1002/adhm.202002254.
[65] R.N. Gomes, F. Manuel, D.S. Nascimento, The bright side of fibroblasts: molecular signature and regenerative cues in major organs, NPJ Regen Med 6 (2021) 1–12, https://doi.org/10.1038/s41536-021-00153-z.
[66] W.G. Stetler-Stevenson, Matrix metalloproteinases in angiogenesis: a moving target for therapeutic intervention, J. Clin. Invest. 103 (1999) 1237–1241, https://doi.org/10.1172/JCI6870.
[67] K. Chen, M. Xu, F. Lu, Y. He, Development of matrix metalloproteinases-mediated extracellular matrix remodeling in regenerative medicine: a mini review, Tissue Eng Regen Med 20 (2023) 661–670, https://doi.org/10.1007/s13770-023-00536-x.
[68] C. Zhou, A.T. Xu, D.D. Wang, G.F. Lin, T. Liu, F.M. He, The effects of Sr-incorporated micro/nano rough titanium surface on rBMSC migration and osteogenic differentiation for rapid osteointegration, Biomater. Sci. 6 (2018) 1946–1961, https://doi.org/10.1039/c8bm00473k.
[69] W. Zhang, H. Cao, X. Zhang, G. Li, Q. Chang, J. Zhao, Y. Qiao, X. Ding, G. Yang, X. Liu, X. Jiang, A strontium-incorporated nanoporous titanium implant surface for rapid osseointegration, Nanoscale 8 (2016) 5291–5301, https://doi.org/10.1039/c5nr08580b.
[70] K. Cui, C.L. Ardell, N.P. Podolnikova, V.P. Yakubenko, Distinct migratory properties of M1, M2, and resident macrophages are regulated by αdβ2and αmβ2integrin-mediated adhesion, Front. Immunol. 9 (2018) 422099, https://doi.org/10.3389/fimmu.2018.02650.
[71] P. Krzyszczyk, R. Schloss, A. Palmer, F. Berthiaume, The role of macrophages in acute and chronic wound healing and interventions to promote pro-wound healing phenotypes, Front. Physiol. 9 (2018) 351269, https://doi.org/10.3389/fphys.2018.00419.
[72] D.R. Griffin, M.M. Archang, C.H. Kuan, W.M. Weaver, J.S. Weinstein, A.C. Feng, A. Ruccia, E. Sideris, V. Ragkousis, J. Koh, M.V. Plikus, D. Di Carlo, T. Segura, P. O. Scumpia, Activating an adaptive immune response from a hydrogel scaffold imparts regenerative wound healing, Nat. Mater. 20 (2021) 560–569, https://doi.org/10.1038/s41563-020-00844-w.
[73] T. Liu, Y. Liu, M. Liu, Y. Wang, W. He, G. Shi, X. Hu, R. Zhan, G. Luo, M. Xing, J. Wu, Synthesis of graphene oxide-quaternary ammonium nanocomposite with synergistic antibacterial activity to promote infected wound healing, Burns Trauma 6 (2018), https://doi.org/10.1186/s41038-018-0115-2.
[74] V.A. Solarte David, V.R. Güiza-Argüello, M.L. Arango-Rodríguez, C.L. Sossa, S. M. Becerra-Bayona, Decellularized tissues for wound healing: towards closing the gap between scaffold design and effective extracellular matrix remodeling, Front. Bioeng. Biotechnol. 10 (2022), https://doi.org/10.3389/FBIOE.2022.821852/FULL.
[75] T. Qian, Z. Li, L. Shang, S. Huang, G. Li, W. Zheng, Y. Mao, pH/temperature responsive curcumin-loaded micelle nanoparticles promote functional repair after spinal cord injury in rats via modulation of inflammation, Tissue Eng Regen Med 20 (2023) 879–892, https://doi.org/10.1007/s13770-023-00567-4.
[76] K. Nuutila, Hair follicle transplantation for wound repair, Adv. Wound Care 10 (2021) 153–163, https://doi.org/10.1089/wound.2019.1139.

[77] A. Kasuya, T. Ito, Y. Tokura, M2 macrophages promote wound-induced hair neogenesis, J. Dermatol. Sci. 91 (2018) 250–255, https://doi.org/10.1016/j.jdermsci.2018.05.004.
[78] I. Pastar, O. Stojadinovic, N.C. Yin, H. Ramirez, A.G. Nusbaum, A. Sawaya, S. B. Patel, L. Khalid, R.R. Isseroff, M. Tomic-Canic, Epithelialization in wound healing: a comprehensive review, Adv. Wound Care 3 (2014) 445–464, https://doi.org/10.1089/wound.2013.0473.
[79] K. Pfisterer, L.E. Shaw, D. Symmank, W. Weninger, The extracellular matrix in skin inflammation and infection, Front. Cell Dev. Biol. 9 (2021) 682414, https://doi.org/10.3389/FCELL.2021.682414/BIBTEX.
[80] G.M. Lee, S. jeong Kim, E.M. Kim, E. Kim, S. Lee, E. Lee, H.H. Park, H. Shin, Free radical-scavenging composite gelatin methacryloyl hydrogels for cell encapsulation, Acta Biomater. 149 (2022) 96–110, https://doi.org/10.1016/j.actbio.2022.06.043.
[81] S. jeong Kim, H. Byun, S. Lee, E. Kim, G.M. Lee, S.J. Huh, J. Joo, H. Shin, Spatially arranged encapsulation of stem cell spheroids within hydrogels for the regulation of spheroid fusion and cell migration, Acta Biomater. 142 (2022) 60–72, https://doi.org/10.1016/j.actbio.2022.01.047.
[82] C. Khatua, S. Min, H.J. Jung, H.J. Jung, H.J. Jung, J.E. Shin, N. Li, I. Jun, H.W. Liu, G. Bae, H. Choi, M.J. Ko, Y.S. Jeon, Y.J. Kim, J. Lee, M. Ko, G. Shim, H. Shin, S. Lee, S. Chung, Y.K. Kim, J.J. Song, V.P. Dravid, V.P. Dravid, V.P. Dravid, H. Kang, In situ magnetic control of macroscale nanoligand density regulates the adhesion and differentiation of stem cells, Nano Lett. 20 (2020) 4188–4196, https://doi.org/10.1021/acs.nanolett.0c00559.
[83] S. Lee, M.S. Kim, K.D. Patel, H. Choi, R. Thangam, J. Yoon, T.M. Koo, H.J. Jung, S. Min, G. Bae, Y. Kim, S.B. Han, N. Kang, M. Kim, N. Li, H.E. Fu, Y.S. Jeon, J. J. Song, D.H. Kim, S. Park, J.W. Choi, R. Paulmurugan, Y.C. Kang, H. Lee, Q. Wei, V.P. Dravid, K.B. Lee, Y.K. Kim, H. Kang, Magnetic control and real-time monitoring of stem cell differentiation by the ligand nanoassembly, Small 17 (2021), https://doi.org/10.1002/smll.202102892.
[84] G. Bae, M.S. Kim, R. Thangam, T.M. Koo, W.Y. Jang, J. Yoon, S.B. Han, L. Yang, S. Y. Kim, N. Kang, S. Min, H. Hong, H.E. Fu, M.J. Ko, D.H. Kim, W.K. Jeong, D. H. Kim, T.H. Kim, J.W. Choi, K.B. Lee, R. Paulmurugan, Y. Zhu, H.J. Kim, J. Lee, J. S. Kim, A. Khademhosseini, Y.K. Kim, H. Kang, Receptor-level proximity and fastening of ligands modulates stem cell differentiation, Adv. Funct. Mater. 32 (2022), https://doi.org/10.1002/adfm.202200828.